Spatio-temporal wavelet regularization for parallel MRI reconstruction: application to functional MRI

Lotfi Chaari, Philippe Ciuciu, Sébastien Mériaux, Jean-Christophe Pesquet

Noname manuscript No.
(will be inserted by the editor)

Spatio-temporal wavelet regularization for parallel MRI reconstruction: application to functional MRI

Lotfi CHAARI[1*], Philippe CIUCIU[2,3], Sébastien MÉRIAUX[2] and Jean-Christophe PESQUET[4]

Word count of abstract : 210

Word count of text : 46050

Number of figures : 12

Number of tables : 6

Number of references : 70

Part of this work has been presented at the IEEE ISBI 2011 conference [1].

The authors would like to thank the CIMI Excellence Laboratory for inviting Philippe Ciuciu on an excellence researcher position during winter and spring 2013.

[1] University of Toulouse, IRIT - INP-ENSEEIHT, France
E-mail: lotfi.chaari@enseeiht.fr
Phone: +33 5 34 32 21 94
Fax: +33 5 34 32 21 57
[2] CEA/NeuroSpin, France
E-mail: firstname.lastname@cea.fr
[3] INRIA Saclay, Parietal, France
[4] LIGM, University Paris-Est, France
E-mail: jean-christophe.pesquet@univ-paris-est.fr
* Corresponding author

Abstract :

Object:

Parallel MRI is a fast imaging technique that helps acquiring highly resolved images in space/time. Its performance depends on the reconstruction algorithm, which can proceed either in the k-space or in the image domain.

Materials and Methods:

To improve the performance of the widely used SENSE algorithm, 2D regularization in the wavelet domain has been investigated. In this paper, we first extend this approach to 3D-wavelet representations and 3D sparsity-promoting regularization term, in order to address reconstruction artifacts which propagate across adjacent slices. The resulting optimality criterion is convex but nonsmooth, and we resort to the Parallel Proximal Algorithm to minimize it. Second, to account for temporal correlation between successive scans in functional MRI (fMRI), we extend our first contribution to 3D+t acquisition schemes by incorporating a prior along the time axis into the objective function.

Results:

Our first method (3D-UWR-SENSE) is validated on T1-MRI anatomical data for gray/white matter segmentation. The second method (4D-UWR-SENSE) is validated for detecting evoked activity during a fast event-related fMRI protocol.

Conclusion:

We show that our algorithm outperforms the SENSE reconstruction at the subject and group levels (15 subjects) for different contrasts of interest (motor or computation tasks) and two parallel acceleration factors ($R = 2$ and $R = 4$) on $2 \times 2 \times 3$ mm^3 EPI images.

Keywords Parallel MRI, fMRI, wavelet transform, spatio-temporal regularization, convex optimization

1 Introduction

Reducing scanning time in Magnetic Resonance Imaging (MRI) exams remains a worldwide challenging issue since it has to be achieved while maintaining high image quality [2, 3]. The expected benefits are *i.)* to limit patient's exposure to the MRI environment either for safety or discomfort reasons, *ii.)* to improve acquisition robustness against subject's motion artifacts and *iii.)* to limit geometric distortions. One basic idea to make MRI acquisitions faster (or to improve spatial resolution in a fixed scanning time) consists of reducing the amount of acquired samples in the k-space (spatial Fourier domain) and developing dedicated reconstruction pipelines. To achieve this goal, three main research avenues have been developed so far:

- *parallel imaging* or parallel MRI that relies on a geometrical principle involving multiple receiver coils with complementary sensitivity profiles. This enables the k-space undersampling along the phase encoding direction without degrading spatial resolution or truncating the Field-Of-View (FOV). pMRI requires the unfolding of reduced FOV coil-specific images to reconstruct the full FOV image [4, 5, 6].
- *Compressed Sensing (CS) MRI* that exploits three ingredients: *sparsity* of MR images in wavelet bases, the *incoherence* between Fourier and inverse wavelet bases which allows to randomly undersample k-space and the *nonlinear recovery* of MR images by solving a convex but nonsmooth ℓ_1 minimization problem [7, 8, 9, 10, 11]. This approach remains usable with classical receiver coil but can also be combined with parallel MRI [12, 13].
- In the dynamic MRI context, fast parallel acquisition schemes have been proposed to increase the acquisition rate by reducing the amount of acquired k-space samples in each frame using interleaved partial k-space sampling between successive frames (UNFOLD approach [14]). To further reduce the scanning time, some strategies taking advantage of both the spatial (actually in

the k-space) and temporal correlations between successive scans in the dataset has been pushed forward such as *kt*-BLAST [15] or *kt*-SPARSE [16].

In parallel MRI (pMRI), many reconstruction methods like SMASH (Simultaneous Acquisition of Spatial Harmonics) [4], GRAPPA (Generalized Autocalibrating Partially Parallel Acquisitions) [6] and SENSE (Sensitivity Encoding) [5] have been proposed in the literature to reconstruct a full FOV image from multiple k-space undersampled images acquired on separate channels. Their main difference lies in the space on which they operate. GRAPPA performs multichannel full FOV reconstruction in the k-space domain whereas SENSE carries out the unfolding process in the image domain: all undersampled images are first reconstructed by inverse Fourier transform before combining them to unwrap the full FOV image. Also, GRAPPA is autocalibrated, whereas SENSE needs a separate coil sensitivity estimation step based on a reference scan. Note however that autocalibrated versions of SENSE are now available such that the `mSENSE` algorithm [17] on Siemens scanners.

In the dynamic MRI context, combined strategies mixing parallel imaging and accelerated sampling schemes along the temporal axis have also been investigated. The corresponding reconstruction algorithms have been referenced to as *kt*-SENSE [15, 18], *kt*-GRAPPA [19]. Compared to `mSENSE` where the centre of the k-space is acquired only once at the beginning, these methods have to acquire the central k-space area at each frame, which decreases the acceleration factor. More recently, optimized versions of *kt*-BLAST and *kt*-SENSE reconstruction algorithms referenced to as *kt*-FOCUSS [20, 21] have been designed to combine the CS theory in space with Fourier or alternative transforms along the time axis. They enable to further reduce data acquisition time without significantly compromising image quality if the image sequence exhibits a high degree of spatio-temporal correlation, either by nature or by design. Typical examples that enter in this context are *i.)* dynamic MRI capturing an organ (liver, kidney, heart) during a quasi-periodic motion due to the respiratory cycle and cardiac beat and *ii.)* functional MRI based on periodic blocked design. However, this interleaved partial *k*-space sampling cannot be exploited in aperiodic dynamic acquisition schemes like in resting state fMRI (rs-fMRI) or during fast-event related fMRI paradigms [22, 23]. In rs-fMRI, spontaneous brain activity is recorded without any experimental design in order to probe intrinsic functional connectivity [22, 24, 25]. In fast event-related designs, the presence of jittering combined with random delivery of stimuli introduces a trial-varying delay between the stimulus and acquisition time points [26]. This prevents the use of an interleaved *k*-space sampling strategy between successive scans since there is no guarantee that the BOLD response is quasi-periodic. Because the vast majority of fMRI studies in neurosciences make use either of rs-fMRI or fast event-related designs [26, 27], the most reliable acquisition strategy in such contexts remains the "scan and repeat" approach, although it is suboptimal. To our knowledge, only one *kt-contribution* (*kt*-GRAPPA [19]) has claimed its ability to accurately reconstruct fMRI images in aperiodic paradigms.

Overview of our contribution

The present paper therefore aims at proposing a new 3D/(3D+t)-dimensional pMRI reconstruction algorithm that can be adopted irrespective of the nature of the encoding scheme or the fMRI paradigm. In particular, we show that our approach outperforms its SENSE-like alternatives not only in terms of artifact removal for anatomical image reconstruction, but also in terms of statistical sensitivity at the subject and group-levels in fast event-related fMRI.

In the fMRI literature, few studies have been conducted to measure the impact of the parallel imaging reconstruction algorithm on EPI volumes and subsequent statistical sensitivity for detecting evoked brain activity [28, 29, 30, 3]. In these works, reliable activations were detected for an acceleration factor up to 3. More recently, a special attention has been paid in [31] to assess the performance of dynamic MRI reconstruction algorithms on BOLD fMRI sensitivity. In [31], the authors have reported that *kt*-based approaches perform better than conventional

SENSE for BOLD fMRI in the sense that reliable sensitivity may be achieved at higher undersampling factors (up to 5). However, most of the time, these comparisons are made on a small group of individuals and statistical analysis is only performed at the subject level. Here, we perform the comparison of several parallel MRI reconstruction algorithms both at the subject and group levels for different acceleration factors.

To remove reconstruction artifacts that occur at high acceleration factors, regularized SENSE methods have been proposed in the literature [32, 33, 34, 35, 36]. Some of them apply quadratic or Total Variation (TV) regularizations while others resort to 2D regularization in the wavelet transform domain (e.g. UWR-SENSE: Unconstrained Wavelet Regularized SENSE) [37]). The latter strategy has proved its efficiency on the reconstruction of anatomical or functional (resting-state only) data, compared to standard SENSE and TV-based regularization [35, 37]. More recently, unconstrained Wavelet Regularized SENSE (or UWR-SENSE) has been assessed on EPI images and compared with `mSENSE` on a brain activation fMRI dataset [38]. This comparison was performed at the subject level only. Besides, except some non-regularized contributions like 3D GRAPPA [39], most of the available reconstruction methods in the literature operate slice by slice and thus reconstruct each slice irrespective of its neighbours. Iterating over slices is thus necessary to recover the whole 3D volume. This observation led us to consider 3D or full FOV image reconstruction as a single step in which all slices are treated together. For doing so, we introduce 3D wavelet transform and 3D sparsity-promoting regularization term in the wavelet domain. This approach can still apply even if the acquisition is performed in 2D instead of 3D. Following the same principle, an fMRI run usually consists of several tens of successive scans that are reconstructed independently one to another. Iterating over all acquired 3D volumes remains the classical approach to reconstruct the 4D or 3D + t dataset. However, it has been shown for a long while that fMRI data are serially correlated in time even under the null hypothesis (i.e., ongoing activity only) [40, 41, 42]. To capture this dependence

between successive time points, an autoregressive model has demonstrated its relevance [43, 44, 45, 46]. Hence, we propose to account for this temporal structure at the reconstruction step.
These two key ideas have played a central role to extend the UWR-SENSE approach [37] through a more general regularization scheme that relies on a convex but nonsmooth criterion to be minimized. This criterion is made up of three terms. The first one (data fidelity) accounts for 3D spatial and temporal dependencies between successive slices and repetitions (i.e., scans) by combining all repetitions and involving a 3D wavelet transform. The second and third terms promote sparsity in the 3D wavelet domain as well as the temporal smoothness of the sought (3D + t) image sequence, respectively. The minimization of this criterion relies on the Parallel ProXimal Algorithm (PPXA) [47] which can address a broader scope of optimization problems than the forward-backward and Douglas-Rachford methods employed in [37], or even FISTA as used in [48].

The rest of this paper is organized as follows. Section 2 recalls the principle of parallel MRI and describes the proposed reconstruction algorithms and optimization aspects. In Section 3, experimental validation of the 3D/4D-UWR-SENSE approaches is performed on anatomical T_1 MRI and BOLD fMRI data, respectively. In Section 4, we discuss the pros and cons of our method. Finally, conclusions and perspectives are drawn in Section 5.

2 Materials and Methods

2.1 Parallel imaging in MRI

In parallel MRI, an array of L coils is employed to indirectly measure the spin density $\overline{\rho} \in \mathbb{R}^{X \times Y}$ [49] within the object under investigation[1]. For Cartesian 2D acquisition schemes, the sampling period along the phase encoding direction is R times larger than the one used for conventional acquisition, $R \leq L$ being the reduc-

[1] The overbar is used to distinguish the "true" data from a generic variable.

tion factor. To recover full FOV images, many algorithms have been proposed but only SENSE-like [5] and GRAPPA-like [6] methods are provided by scanner manufacturers. For more details about the parallel MRI formalism, interested readers can refer to [49, 5, 6, 37]. In what follows, we focus on SENSE-like methods operating in the image domain. Under coil-dependent additive zero-mean Gaussian noise assumptions, and denoting by $\boldsymbol{r} = (x, y)^{\mathsf{T}} \in X \times Y$ the spatial position in the image domain ($\cdot^{\mathsf{T}}$ being the transpose operator), SENSE amounts to solving the following one-dimensional inversion problem at each spatial position $\boldsymbol{r} = (x, y)^{\mathsf{T}}$ [5, 37]:

$$\boldsymbol{d}(\boldsymbol{r}) = \boldsymbol{S}(\boldsymbol{r})\overline{\boldsymbol{\rho}}(\boldsymbol{r}) + \boldsymbol{n}(\boldsymbol{r}), \tag{1}$$

where $\boldsymbol{n}(\boldsymbol{r})$ $(L \times 1)$ is the noise term, $\boldsymbol{d}$ $(L \times 1)$ the acquired signal and $\overline{\boldsymbol{\rho}}$ $(R \times 1)$ the target image. The *sensitivity* matrix $\boldsymbol{S}$ $(L \times R)$ is estimated using a reference scan and varies according to the coil geometry. Note that the coil images as well as the sought image $\overline{\rho}$ are complex-valued, although $|\overline{\rho}|$ is only considered for visualization purposes. Indeed, keeping the complex nature of the data allows accounting for both magnitde and phase of the acquired signals. The phase signal in MRI has been demonstrated to be informative in some recent studies such as [50].

The 1D-SENSE reconstruction method [5] actually minimizes a Weighted Least Squares (WLS) criterion $\mathcal{J}_{\mathrm{WLS}}$ given by:

$$\mathcal{J}_{\mathrm{WLS}}(\rho) = \sum_{\mathbf{r} \in \{1,\ldots,X\} \times \{1,\ldots,Y/R\}} \| \boldsymbol{d}(\boldsymbol{r}) - \boldsymbol{S}(\boldsymbol{r})\boldsymbol{\rho}(\boldsymbol{r}) \|^2_{\boldsymbol{\Psi}^{-1}}, \tag{2}$$

where $\boldsymbol{\Psi}$ is the noise covariance matrix and $\| \cdot \|_{\boldsymbol{\Psi}^{-1}} = \sqrt{(\cdot)^{\mathsf{H}}\boldsymbol{\Psi}^{-1}(\cdot)}$. Hence, the SENSE full FOV image is nothing but the maximum likelihood estimate which admits the following closed-form expression at each spatial position $\boldsymbol{r}$:

$$\widehat{\boldsymbol{\rho}}_{\mathrm{WLS}}(\boldsymbol{r}) = \left(\boldsymbol{S}^{\mathsf{H}}(\boldsymbol{r})\boldsymbol{\Psi}^{-1}\boldsymbol{S}(\boldsymbol{r})\right)^{\sharp} \boldsymbol{S}^{\mathsf{H}}(\boldsymbol{r})\boldsymbol{\Psi}^{-1}\boldsymbol{d}(\boldsymbol{r}), \tag{3}$$

where $(\cdot)^{\mathsf{H}}$ (respectively $(\cdot)^{\sharp}$) stands for the transposed complex conjugate (respectively pseudo-inverse). It should be noticed here that the described 1D-SENSE reconstruction method has been designed to reconstruct one slice (2D image). To reconstruct a full volume, the 1D-SENSE reconstruction algorithm has to be iterated over all slices. In practice, the performance of the SENSE method is limited because of *i)* different sources of noise such as distortions in the measurements $\boldsymbol{d}(\boldsymbol{r})$, and *ii)* distortions in estimation and ill-conditioning of $\boldsymbol{S}(\boldsymbol{r})$ mainly at brain/air interfaces. To enhance the robustness of the solution to this ill-posed problem, a regularization is usually introduced in the reconstruction process. To go beyond the over-smoothing effects of quadratic regularization [32, 33], edge-preserving penalties have been widely investigated in the pMRI reconstruction literature. For instance, the Total Variation (TV) regularization has been proposed in recent works [51, 52]. However, TV is mostly adapted to piecewise constant images, which doesn't reflect the prior knowledge in fMRI. As investigated by *Chaari et al.* [37], *Liu et al.* [36] and *Guerquin-Kern et al.* [48], regularization in the Wavelet Transform (WT) domain is a powerful tool to improve SENSE reconstruction. In what follows, we summarize the principles of wavelet-based regularization.

2.2 Proposed wavelet-based regularized SENSE

Akin to [37] where a regularized reconstruction algorithm relying on 2D separable WTs was investigated, to the best of our knowledge, all the existing approaches in the pMRI regularization literature proceed slice by slice. The drawback of this strategy is that no spatial continuity between adjacent slices is taken into account. Similarly in fMRI, the whole brain volume is acquired repeatedly during an fMRI run. Hence, it becomes necessary to iterate over all volumes to reconstruct 4D datasets. Consequently, the 3D volumes are supposed independent in time whereas it is known that fMRI time-series are serially correlated [43] because of two distinct effects: the BOLD signal itself is a low-pass filtered version of the neural activity, and physiological artifacts make the fMRI time series strongly dependent. For these reasons, modeling temporal dependence across scans at the reconstruction step may impact subsequent statistical analysis. This has motivated the extension of the wavelet regularized reconstruction approach in [37] in order to:

– account for 3D spatial dependencies between adjacent slices by using 3D WTs,
– exploit the temporal dependency between acquired 3D volumes by applying an additional regularization term along the temporal dimension of the 4D dataset.

This additional regularization will help us in increasing the Signal to Noise Ratio (SNR) through the acquired volumes, and therefore enhance the reliability of the statistical analysis in fMRI. These temporal dependencies have also been used in the dynamic MRI literature in order to improve the reconstruction quality in conventional MRI [53]. However, since the imaged object geometry in the latter context generally changes during the acquisition, taking the temporal regularization in the reconstruction process into account becomes very difficult. An optimal design of 3D reconstruction should integrate slice-timing and motion correction in the reconstruction pipeline. For the sake of computational efficiency, our approach only performs 3D reconstruction before considering slice-timing and motion correction. To deal with a 4D reconstruction of the N_r acquired volumes, we will first rewrite the observation model in Eq. (1) as follows:

$$\boldsymbol{d}^t(\boldsymbol{r}) = \boldsymbol{S}(\boldsymbol{r})\boldsymbol{\rho}^t(\boldsymbol{r}) + \boldsymbol{n}^t(\boldsymbol{r}), \tag{4}$$

where $t \in \{1, \dots, N_r\}$ is the frame index and $\boldsymbol{r} = (x, y, z)$ is the 3D spatial position, $z \in \{1, \dots, Z\}$ being the slice index. At a given frame t, the full FOV 3D complex-valued image $\overline{\rho}^t$ of size $X \times Y \times Z$ can be seen as an element of the Euclidean space $\mathbb{C}^K$ with $K = X \times Y \times Z$ endowed with the standard inner product $\langle \cdot \mid \cdot \rangle$ and norm $\| \cdot \|$. We employ a dyadic 3D orthonormal wavelet decomposition operator T over $j_{\max}$ resolution levels (typically 3 as used in our results). To perform 3D wavelet decomposition using a given filter (*Symmlet* for instance), the same filter is applied across lines (X), columns (Y) and slices (Z). The coefficient field resulting from the wavelet decomposition of a target image ρ^t is defined as $\zeta^t = \big(\boldsymbol{\zeta}_a^t, (\boldsymbol{\zeta}_{o,j}^t)_{o \in \mathbb{O}, 1 \leq j \leq j_{\max}}\big)$ with $o \in \mathbb{O} = \{0,1\}^3 \backslash \{(0,0,0)\}$, $\boldsymbol{\zeta}_a^t = (\zeta_{a,k}^t)_{1 \leq k \leq K_{j_{\max}}}$

and $\boldsymbol{\zeta}_{o,j}^t = (\zeta_{o,j,k}^t)_{1\leq k\leq K_j}$ where $K_j = K2^{-3j}$ is the number of wavelet coefficients in a given subband at resolution j (by assuming that X, Y and Z are multiple of $2^{j_{\max}}$). Note that if the image size is not a power of 2, and as usually performed in the wavelet literature, zero-padding can be used for example to reach a power of 2 matrix size.

Adopting such a notation, the wavelet coefficients have been reindexed so that $\boldsymbol{\zeta}_a^t$ denotes the approximation coefficient vector at the resolution level $j_{\max}$, while $\boldsymbol{\zeta}_{o,j}^t$ denotes the detail coefficient vector at the orientation o and resolution level j. Using 3D dyadic WTs allows us to smooth reconstruction artifacts along the slice selection direction that may appear at the same spatial position, which is not possible using a slice by slice processing. Also, even if reconstruction artifacts do not exactly appear in the same positions, the proposed method allows us to incorporate reliable information from adjacent slices in the reconstruction model.

The proposed regularization procedure relies on the introduction of two penalty terms. The first penalty term describes the prior 3D spatial knowledge about the wavelet coefficients of the target solution and it is expressed as:

$$g(\zeta) = \sum_{t=1}^{N_r} \Big[\sum_{k=1}^{K_{j_{\max}}} \Phi_a(\zeta_{a,k}^t) + \sum_{o\in\mathbb{O}} \sum_{j=1}^{j_{\max}} \sum_{k=1}^{K_j} \Phi_{o,j}(\zeta_{o,j,k}^t)\Big], \tag{5}$$

where $\zeta = (\zeta^1, \zeta^2, \ldots, \zeta^{N_r})$ and we have, for every $o \in \mathbb{O}$ and $j \in \{1, \ldots, j_{\max}\}$ (and similarly for Φ_a relative to the approximation coefficients),

$$\forall \xi \in \mathbb{C}, \qquad \Phi_{o,j}(\xi) = \Phi_{o,j}^{\mathrm{Re}}(\xi) + \Phi_{o,j}^{\mathrm{Im}}(\xi) \tag{6}$$

where $\Phi_{o,j}^{\mathrm{Re}}(\xi) = \alpha_{o,j}^{\mathrm{Re}}|\mathrm{Re}(\xi - \mu_{o,j})| + \frac{\beta_{o,j}^{\mathrm{Re}}}{2}|\mathrm{Re}(\xi - \mu_{o,j})|^2$ and $\Phi_{o,j}^{\mathrm{Im}}(\xi) = \alpha_{o,j}^{\mathrm{Im}}|\mathrm{Im}(\xi - \mu_{o,j})| + \frac{\beta_{o,j}^{\mathrm{Im}}}{2}|\mathrm{Im}(\xi - \mu_{o,j})|^2$ with $\mu_{o,j} = \mu_{o,j}^{\mathrm{Re}} + \imath\mu_{o,j}^{\mathrm{Im}} \in \mathbb{C}$, and $\alpha_{o,j}^{\mathrm{Re}}$, $\beta_{o,j}^{\mathrm{Re}}$, $\alpha_{o,j}^{\mathrm{Im}}$, $\beta_{o,j}^{\mathrm{Im}}$ are some positive real constants. Hereabove, $\mathrm{Re}(\cdot)$ and $\mathrm{Im}(\cdot)$ (or $\cdot^{\mathrm{Re}}$ and $\cdot^{\mathrm{Im}}$) stand for the real and imaginary parts, respectively. For both real and imaginary parts, this regularization term allows us to keep a compromise between sparsity and smoothness of the wavelet coefficients due to the ℓ_1 and ℓ_2 terms, respectively. This $\ell_1 - \ell_2$

regularization is therefore more flexible and can model a larger panel of images than a simple ℓ_1 regularization. The usefulness of this kind of penalization has been demonstrated in [37].

The second regularization term penalizes the temporal variation between successive 3D volumes:

$$h(\zeta) = \kappa \sum_{t=2}^{N_r} \|T^*\zeta^t - T^*\zeta^{t-1}\|_p^p \tag{7}$$

where T^* is the 3D wavelet reconstruction operator. The prior parameters $\boldsymbol{\alpha}_{o,j} = (\alpha_{o,j}^{\text{Re}}, \alpha_{o,j}^{\text{Im}})$, $\boldsymbol{\beta}_{o,j} = (\beta_{o,j}^{\text{Re}}, \beta_{o,j}^{\text{Im}})$, $\boldsymbol{\mu}_{o,j} = (\mu_{o,j}^{\text{Re}}, \mu_{o,j}^{\text{Im}})$, $\kappa \in [0, +\infty[$ and $p \in [1, +\infty[$ are unknown and they need to be estimated. The used ℓ_p norm gives more flexibility to the temporal penalization term by allowing it to promote different levels of sparsity depending on the value of p. Such a penalization has been chosen based on empirical studies that have been conducted on the time-course of the BOLD signal at the voxel level. This parameter has been finally fixed to $p = 1$.

Based on the formulation hereabove, the criterion to be minimized in order to get the 4D-UWR-SENSE solution can be written as follows:

$$\mathcal{J}_{\text{ST}}(\zeta) = \mathcal{J}_{\text{TWLS}}(\zeta) + g(\zeta) + h(\zeta) \tag{8}$$

where $\mathcal{J}_{\text{TWLS}}$ is defined as

$$\begin{aligned}\mathcal{J}_{\text{TWLS}}(\zeta) &= \sum_{t=1}^{N_r} \mathcal{J}_{\text{WLS}}(\zeta^t) \\ &= \sum_{t=1}^{N_r} \sum_{\mathbf{r} \in \{1,\ldots,X\} \times \{1,\ldots,Y/R\} \times \{1,\ldots,Z\}} \|\boldsymbol{d}^t(\boldsymbol{r}) - \boldsymbol{S}(\boldsymbol{r})(T^*\zeta^t)(\boldsymbol{r})\|_{\boldsymbol{\Psi}^{-1}}^2 .\end{aligned} \tag{9}$$

If only the 3D spatial regularization is considered, the 3D-UWR-SENSE solution is obtained by minimizing the following criterion for every acquisition frame $t = 1 \ldots N_r$:

$$\mathcal{J}_{\text{S}}(\zeta^t) = \mathcal{J}_{\text{WLS}}(\zeta^t) + g_s(\zeta^t), \tag{10}$$

where $\mathcal{J}_{\mathrm{WLS}}$ is defined in Eq. (2) and g_s is defined as

$$g_s(\zeta^t) = \sum_{k=1}^{K_{j_{\max}}} \Phi_a(\zeta^t_{a,k}) + \sum_{o\in\mathbb{O}} \sum_{j=1}^{j_{\max}} \sum_{k=1}^{K_j} \Phi_{o,j}(\zeta^t_{o,j,k}). \quad (11)$$

The operator T^* is then applied to each component ζ^t of ζ to obtain the reconstructed 3D volume ρ^t related to acquisition frame t. It should be noticed here that other choices for the penalty functions are also possible provided that the convexity of the resulting optimality criterion is ensured. This condition enables the use of fast and efficient convex optimization algorithms. Adopting this formulation, the minimization procedure plays a prominent role in the reconstruction process. The proposed optimization procedure is detailed in Appendix A.

3 Results

This section is dedicated to the experimental validation of the reconstruction algorithm we proposed in Section 2.2. Experiments have been conducted on both anatomical and functional data which was acquired on a 3T Siemens Trio magnet. For fMRI acquisition, ethics approval was delivered by the local research ethics committee (Kremlin-Bicêtre, CPP: 08 032) and fifteen volunteers gave their written informed consent for participation.

For anatomical data, the proposed 3D-UWR-SENSE algorithm (4D-UWR-SENSE without temporal regularization) is compared to the scanner reconstruction pipeline. As regards fMRI validation, results of subject and group-level fMRI statistical analyses are compared for two reconstruction pipelines: the one available on the scanner workstation and our own pipeline which, for the sake of completeness, involves either the early UWR-SENSE [37] or the 4D-UWR-SENSE version of the proposed pMRI reconstruction algorithm.

3.1 Anatomical data

Anatomical data has been acquired using a 3D T_1-weighted MP-RAGE pulse sequence at a $1 \times 1 \times 1.1$ mm^3 spatial resolution (TE = 2.98 ms, TR = 2300 ms, TI = 900 ms, flip angle = 9°, slice thickness = 1.1 mm, transversal orientation, FOV = $256 \times 240 \times 176$ mm^3, TR between two RF pulses: 7.1 ms, antero-posterior phase encoding). Data has been collected using a 32-channel receiver coil (no parallel transmission) at two different acceleration factors, $R = 2$ and $R = 4$.

To compare the proposed approach to the `mSENSE` [2] one, Fig. 1 illustrates coronal anatomical slices reconstructed with both algorithms while turning off the temporal regularization in 4D-UWR-SENSE. Red circles clearly show reconstruction artifacts and noise in the `mSENSE` reconstruction, which have been removed using our 3D-UWR-SENSE approach. Comparison may also be made through reconstructed slices for $R = 2$ and $R = 4$, as well as with the conventional acquisition ($R = 1$). This figure shows that increasing R generates more noise and artifacts in `mSENSE` results whereas the impact on our results is attenuated. Artifacts are smoothed by using the continuity of spatial information across contiguous slices in the wavelet space. Depending on the used wavelet basis and the number of vanishing moments, more or less (4 or 8 for instance) adjacent slices are involved in the reconstruction of a given slice. Here we used Symmlet filters of length 8 (4 vanishing moments) which makes 8 adjacent slices involved in the reconstruction of a given slice. The smoothing level inherent to the proposed method strongly depends on the regularization parameters that are used to set the thresholding level of wavelet coefficients. Images reconstructed using our algorithm present higher smoothing level than `mSENSE` without altering key information in the images. When carefully analysing the image background, one can notice the presence of motion-like artifacts that only affect the background and do not alter the brain mask. Such artifacts are nothing but boundary effects due to the use of wavelet transforms. Note also that `mSENSE` images present higher contrast level, which is due to the

[2] SENSE reconstruction implemented by the Siemens scanner, software ICE, VB 17.

contrast homogenization step applied by the scanner manufacturer. Our pipeline does not involve any contrast homogenization in order to preserve data integrity.

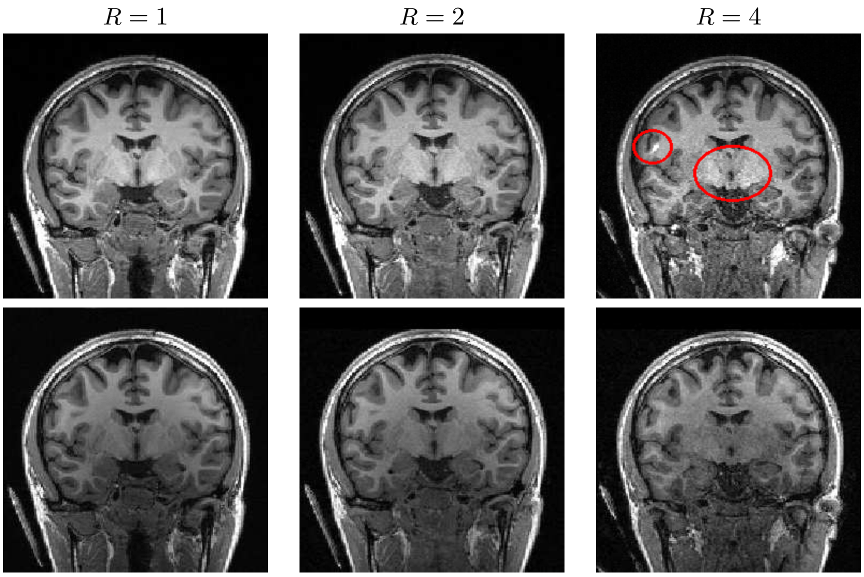

Fig. 1 **Coronal** reconstructed slices using `mSENSE` (top row) and 3D-UWR-SENSE (bottom row) for $R = 2$ and $R = 4$ with $1 \times 1 \times 1.1$ mm^3 spatial resolution. Reconstructed slices are also provided for a conventional acquisition (non accelerated with $R = 1$) as the Sum Of Squares (SOS). Red ellipsoids indicate the position of reconstruction artifacts using `mSENSE`.

In order to evaluate the impact of such smoothing, classification tests have been conducted based on images reconstructed with both methods. Gray and white matter classification results using the Morphologist 2012 pipeline of T_1-MRI toolbox of Brainvisa software[3] at $R = 2$ and $R = 4$ are compared to those obtained without acceleration (i.e. at $R = 1$), considered as the ground truth. Displayed results in Fig. 2 show that classification errors occur close to reconstruction artifacts for `mSENSE`, especially at $R = 4$. The obtained results using our 3D-UWR-SENSE algorithm show that the gray matter is better classified especially close to the artifact into the red circle (left red circle in Fig. 2 [$R = 4$]), which lies at the frontier between the white and gray matters. Moreover, reconstruction noise with

[3] http://brainvisa.info

mSENSE in the centre of the white matter (right red circle in Fig 2 [$R = 4$]) also causes miss-classification errors far from the gray/while matter frontier. However, at $R = 1$ and $R = 2$ classification performance is rather similar for both methods, which confirms the ability of the proposed method to attenuate reconstruction artifacts while keeping classification results unbiased.

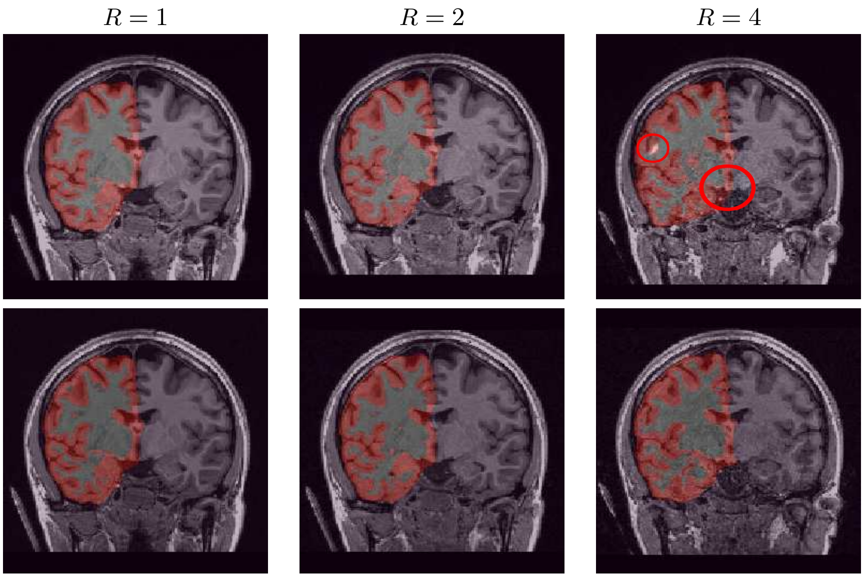

Fig. 2 Coronal view of classification results based on reconstructed slices using mSENSE (top row) and 3D-UWR-SENSE (bottom row) for $R = 2$ and $R = 4$ with $1 \times 1 \times 1.1$ mm^3 spatial resolution. Classification results based on the SOS of a non-accelerated acquisition ($R = 1$) are also provided as a ground truth. Red circles indicate the position of reconstruction artifacts using mSENSE for $R = 4$.

To further investigate the smoothing effect of our reconstruction algorithm, gray matter interface of the cortical surface has bee extracted using the above mentioned BrainVISA pipeline. Extracted surfaces (medial and lateral views) from mSENSE and 3D-UWR-SENSE images are show in Fig. 3 for $R = 4$. For comparison purpose, we provide results with mSENSE at $R = 1$ as ground truth. For the lateral view, one can easily conclude that extracted surfaces are very similar. However, the medial view shows that mSENSE is not able to correctly segment the brain-stem (see right red ellipsoid in the mSENSE medial view). Moreover, results with

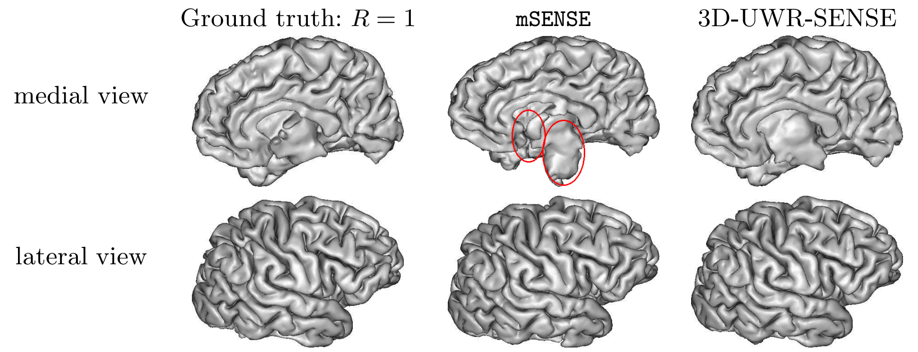

Fig. 3 Gray matter surface extraction based on reconstructed slices using `mSENSE` and 3D-UWR-SENSE for $R = 4$. Results obtained with $R = 1$ are also provided as a ground truth.

`mSENSE` are more noisy compared to 3D-UWR-SENSE (see left red ellipsoid in the `mSENSE` medial view). In contrast, the calcarine sulcus is slightly less accurately extracted by our approach.

It is worth noticing that similar results have been obtained on 14 other subjects.

3.2 Functional datasets

For fMRI data, a Gradient-Echo EPI (GE-EPI) sequence has been used (TE = 30 ms, TR = 2400 ms, slice thickness = 3 mm, transversal orientation, FOV = 192×192 mm^2, flip angle = 81°) during a cognitive *localizer* [54] protocol. Slices have been collected in a sequential order (slice n°1 in feet, last slice to head) using the same 32-channel receiver coil to cover the whole brain in 39 slices for the two acceleration factors $R = 2$ and $R = 4$. This leads to a spatial resolution of $2 \times 2 \times 3$ mm^3 and a data matrix size of $96 \times 96 \times 39$ for accelerated acquisitions.

This experiment has been designed to map auditory, visual and motor brain functions as well as higher cognitive tasks such as number processing and language comprehension (listening and reading). It consisted of a single session of $N_r = 128$ scans. The paradigm was a fast event-related design (ISI=3.75 s) comprising sixty auditory, visual and motor stimuli, defined in ten experimental conditions (auditory and visual sentences, auditory and visual calculations, left/right auditory and visual clicks, horizontal and vertical checkerboards). Since data at $R = 1$, $R = 2$ and $R = 4$ were acquired for each subject, acquisition orders have been equally balanced between these three reduction factors over the fifteen subjects.

3.2.1 FMRI reconstruction pipeline

For each subject, fMRI data were collected at the 2×2 mm^2 spatial in-plane resolution using different reduction factors ($R = 2$ or $R = 4$). Based on the raw data files delivered by the scanner, reduced FOV EPI images were reconstructed as detailed in Fig. 4. This reconstruction is performed in two stages:

i) the *1D k-space regridding* (blip gradients along phase encoding direction applied in-between readout gradients) to account for the non-uniform k-space sampling during readout gradient ramp, which occurs in fast MRI sequences like GE-EPI;

ii) the *Nyquist ghosting correction* to remove the odd-even echo inconsistencies during k-space acquisition of EPI images.

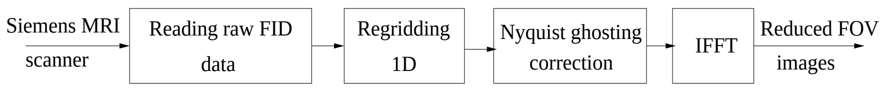

Fig. 4 Reconstruction pipeline of reduced FOV EPI images from the raw FID data.

It must be emphasized here that since no interleaved k-space sampling is performed during the acquisition, and since the central lines of the k-space are not acquired for each TR due to the available imaging sequences on the Siemens scanner, kt-FOCUSS-like methods are not applicable on the available dataset.

Once the reduced FOV images are available, the proposed pMRI 4D-UWR-SENSE algorithm and its early UWR-SENSE version have been utilized in a final step to reconstruct the full FOV EPI images and compared to the `mSENSE` solution. For the wavelet-based regularization, dyadic *Symmlet* orthonormal wavelet bases [55] associated with filters of length 8 have been used over $j_{\max} = 3$ resolution levels.

The reconstructed EPI images then enter in our fMRI study in order to measure the impact of the reconstruction method choice on brain activity detection. Note also that the proposed reconstruction algorithm requires the estimation of the coil sensitivity maps (matrix $\boldsymbol{S}(\cdot)$ in Eq. (1)). As proposed in [5], the latter were estimated by dividing the coil-specific images by the module of the Sum Of Squares (SOS) images, which are computed from the specific acquisition of the k-space centre (24 lines) before the N_r scans. The same sensitivity map estimation is then used for all the compared methods. Fig. 5 compares the two pMRI reconstruction algorithms to illustrate on axial, coronal and sagittal EPI slices how the `mSENSE` reconstruction artifacts have been removed using the 4D-UWR-SENSE approach. Reconstructed `mSENSE` images actually present large artifacts located both at the centre and boundaries of the brain in sensory and cognitive regions (temporal lobes, frontal and motor cortices, ...). This results in SNR loss and thus may have a dramatic impact for activation detection in these brain regions. Note that these conclusions are reproducible across subjects although the artifacts may appear on different slices (see red circles in Fig. 5). One can also notice that some residual artifacts still exist in the reconstructed images with our pipeline especially for $R = 4$. Such strong artifacts are only attenuated and not fully removed because of the high level of information loss at $R = 4$.

Regarding computational load, the `mSENSE` algorithm is carried out on-line and remains compatible with real time processing. On the other hand, our pipeline is carried out off-line and requires more computations. For illustration purpose, on a biprocessor quadcore `Intel Xeon CPU`@ 2.67GHz, one EPI slice is reconstructed in 4 s using the UWR-SENSE algorithm. Using parallel computing strategy and multithreading (through the `OMP` library), each EPI volume consisting of 40 slices is reconstruced in 22 s. This makes the whole series of 128 EPI images available in about 47 min. By contrast, the proposed 4D-UWR-SENSE achieves the reconstruction of the series in about 40 min, but requires larger memory space

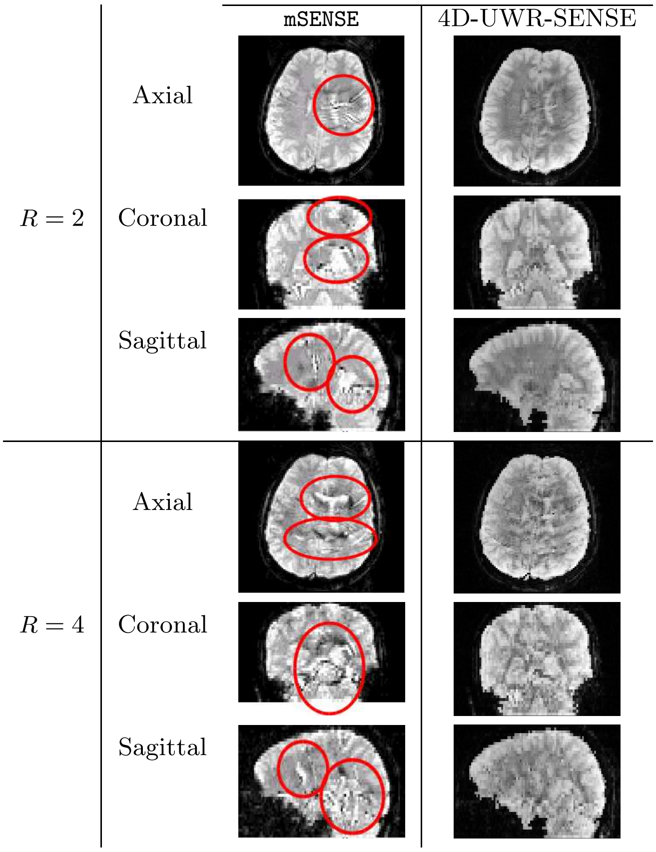

Fig. 5 **Axial**, **Coronal** and **Sagittal** reconstructed slices using `mSENSE` and 4D-UWR-SENSE for $R = 2$ and $R = 4$ with 2×2 mm^2 in-plane spatial resolution. Red circles and ellipsoids indicate the position of reconstruction artifacts using `mSENSE`.

3.2.2 Subject-level analysis

Statistical fMRI data analyses have been conducted to investigate the impact of the proposed reconstruction method on the sensitivity/specificity compromise of brain activity detection. Before handling the statistical analysis using the SPM software[4], full FOV fMRI images were preprocessed using the following steps: *i)* realignment, *ii)* slice-timing correction, *iii)* anatomo-functional coregistration, *iv)* spatial normalization (for group-level analysis), and *v)* smoothing with an isotropic Gaussian kernel of 4 mm full-width at half-maximum. Anatomical normalization

[4] http://www.fil.ion.ucl.ac.uk/spm/software/spm5

to the MNI[5] space was performed on the coregistration of the functional images with the anatomical T_1 scan (using SPM5).

A General Linear Model (GLM) was then constructed to capture stimulus-related BOLD response. As shown in Fig. 6, the design matrix relies on ten experimental conditions and is thus made up of twenty one regressors corresponding to stick functions convolved with the canonical Haemodynamic Response Function (HRF) and its first temporal derivative, the last regressor modelling the baseline. This GLM was then fitted to the same acquired images but reconstructed using either `mSENSE` or our own pipeline, which in the following is derived from the early UWR-SENSE method [37] and from its 4D-UWR-SENSE extension we propose here. The estimated contrast images for motor responses and higher cognitive

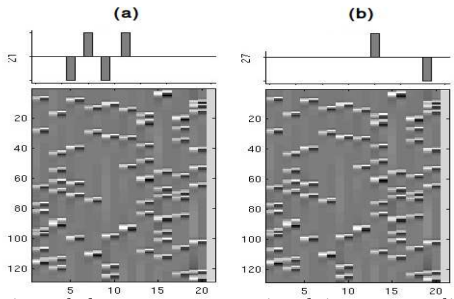

Fig. 6 (a): Design matrix and the `Lc-Rc` contrast involving two conditions (grouping auditory and visual modalities); (b): design matrix and the `Ac-As` contrast involving four conditions (sentence, computation, left click, right click).

functions (computation, language) where entered in subsequent analysis. These contrasts of interest are complementary since the expected activations lie in different brain regions and thus can be differentially corrupted by reconstruction artifacts as outlined in Fig. 5. More precisely, we studied:

– the **Left click vs. Right click** (`Lc-Rc`) contrast for which we expect evoked activity in the right motor cortex (precentral gyrus, middle frontal gyrus). Indeed, the `Lc-Rc` contrast defines a compound comparison involving two motor stimuli which are presented either in the visual or auditory modality. This

[5] Montreal Neurological Institute

comparison aims therefore at detecting lateralization effect in the motor cortex: see Fig. 6(a).

– the **Auditory computation vs. Auditory sentence** (`Ac-As`) contrast which is supposed to elicit evoked activity in the frontal and parietal lobes, since solving mental arithmetic task involves working memory and more specifically the intra-parietal sulcus [56]: see Fig. 6(b);

Interestingly, these two contrasts were chosen because they summarized well different situations (large vs small activation clusters, distributed vs focal activation pattern, bilateral vs unilateral activity) that occurred for this paradigm when looking at sensory areas (visual, auditory, motor) or regions involved in higher cognitive functions (reading, calculation). In the following, our results are reported in terms of Student's t-maps thresholded at a cluster-level $p = 0.05$ corrected for multiple comparisons according to the FamilyWise Error Rate (FWER) [57, 58]. Complementary statistical tables provide corrected cluster and voxel-level p-values, maximal t-scores and corresponding peak positions both for $R = 2$ and $R = 4$. Note that clusters are listed in a decreasing order of significance. In this table, *Size* refers the cluster size in 3D and *Position* denotes the position of the absolute maximum of the related cluster in millimeters (in the normalized MNI template space). As regards the *T-score*, it denotes the Student-t statistical score.

Concerning the `Lc-Rc` contrast on the data acquired with $R = 2$, Fig. 7 [top] shows that all reconstruction methods enable to retrieve the expected activation in the right precentral gyrus. However, when looking more carefully at the statistical results (see Tab. 1), our pipeline and especially the 4D-UWR-SENSE algorithm retrieves an additional cluster in the right middle frontal gyrus. On data acquired with $R = 4$, the same `Lc-Rc` contrast elicits similar activations, i.e. in the same region. As demonstrated in Fig. 7 [bottom], this activity is enhanced when pMRI reconstruction is performed with our pipeline. Quantitative results in Tab. 1 confirm numerically what can be observed in Fig. 7: larger clusters with higher local t-scores are detected using the 4D-UWR-SENSE algorithm, both for $R = 2$ and

$R = 4$. Also, a larger number of clusters is retrieved for $R = 2$ using wavelet-based regularization.

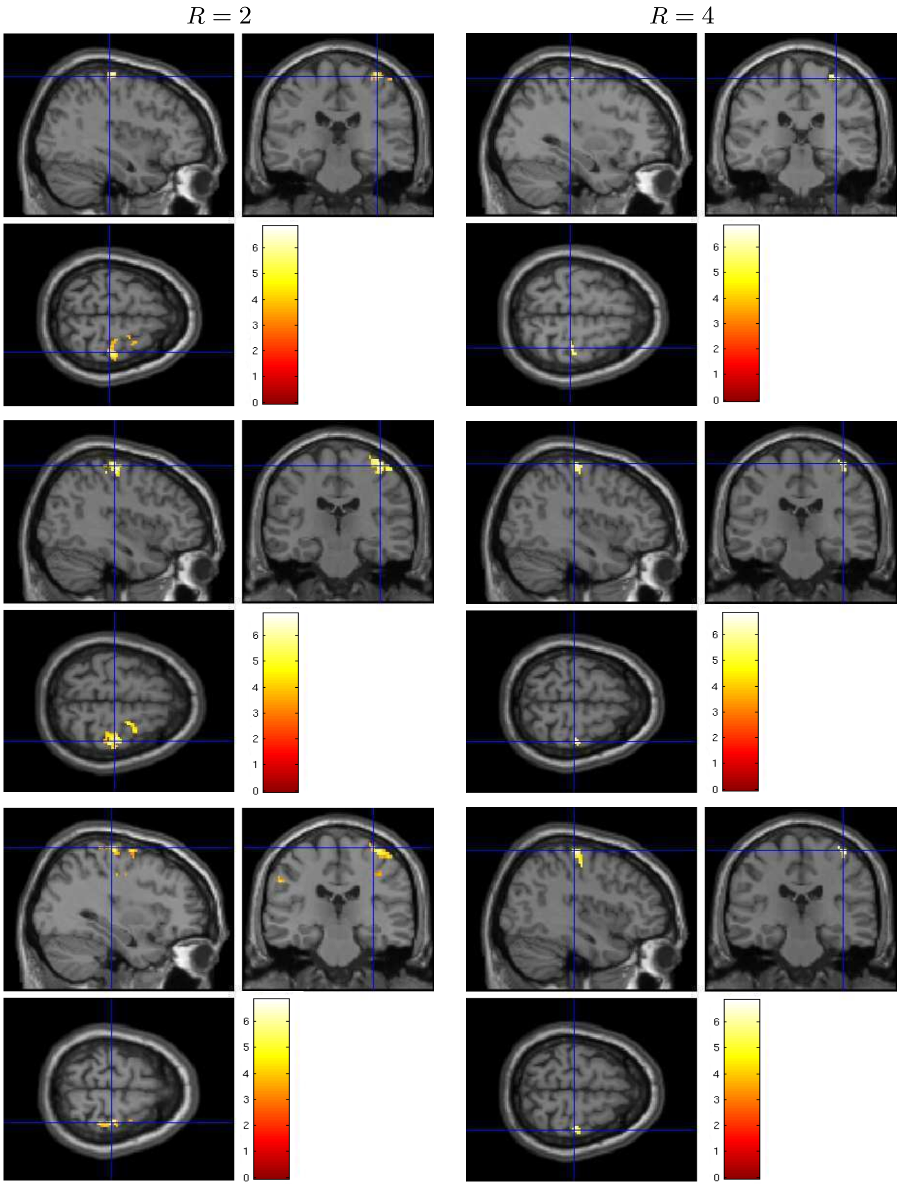

Fig. 7 Student's t-maps superimposed to anatomical MRI for the `Lc-Rc` contrast. Data have been reconstructed using the `mSENSE` (top row), UWR-SENSE (middle row) and 4D-UWR-SENSE (bottom row), respectively. Neurological convention. The blue cross shows the global maximum activation peak.

Table 1 Significant statistical results at the subject-level for the `Lc-Rc` contrast (corrected for multiple comparisons at $p = 0.05$). Images were reconstructed using the `mSENSE`, UWR-SENSE and 4D-UWR-SENSE (with and without spatial smoothing for the latter) algorithms for $R = 2$ and $R = 4$.

		cluster-level		voxel-level		
		p-value	Size	p-value	T-score	Position
$R = 2$	`mSENSE`	$< 10^{-3}$	79	$< 10^{-3}$	6.49	38 -26 66
$R = 2$	UWR-SENSE	$< 10^{-3}$	144	0.004	5.82	40 -22 63
$R = 2$	UWR-SENSE	0.03	21	0.064	4.19	24 -8 63
$R = 2$	4D-UWR-SENSE	$< 10^{-3}$	**189**	0.001	**7.03**	34 -24 69
$R = 2$	4D-UWR-SENSE	$< 10^{-3}$	53	0.001	4.98	50 -18 42
$R = 2$	4D-UWR-SENSE	$< 10^{-3}$	47	0.001	5.14	32 -6 66
$R = 4$	`mSENSE`	0.006	21	0.295	4.82	34 -28 63
$R = 4$	UWR-SENSE	$< 10^{-3}$	33	0.120	5.06	40 -24 66
$R = 4$	4D-UWR-SENSE	$< 10^{-3}$	**51**	0.006	**5.57**	40 -24 66

Fig. 8 reports outlines that the proposed pMRI pipeline is robust to the between-subject variability for this motor contrast. Since sensory functions are expected to generate larger BOLD effects (higher SNR) and appear more stable, our comparison takes only place at $R = 4$. The Student's t-maps for two individuals are compared in Fig. 8. For the second subject, one can observe that the `mSENSE` algorithm fails to detect any activation cluster in the right motor cortex. In contrast, our 4D-UWR-SENSE method retrieves more coherent activity for this second subject in the expected region.

For the `Ac-As` contrast, Fig. 9 [top] shows, for the most significant slice and $R = 2$, that all pMRI reconstruction algorithms succeed in finding evoked activity in the left parietal and frontal cortices, more precisely in the inferior parietal lobule and middle frontal gyrus according to the AAL template[6]. Tab. 2 also confirms a bilateral activity pattern in parietal regions for $R = 2$. Moreover, for $R = 4$, Fig. 9 [bottom] illustrates that our pipeline (UWR-SENSE and 4D-UWR-SENSE) and especially the proposed 4D-UWR-SENSE scheme enables to retrieve reliable frontal activity elicited by mental calculation, which is lost by the the `mSENSE` algorithm. From a quantitative viewpoint, the proposed 4D-UWR-SENSE algorithm finds larger clusters whose local maxima are more significant than the

[6] available in the `xjView` toolbox of SPM5.

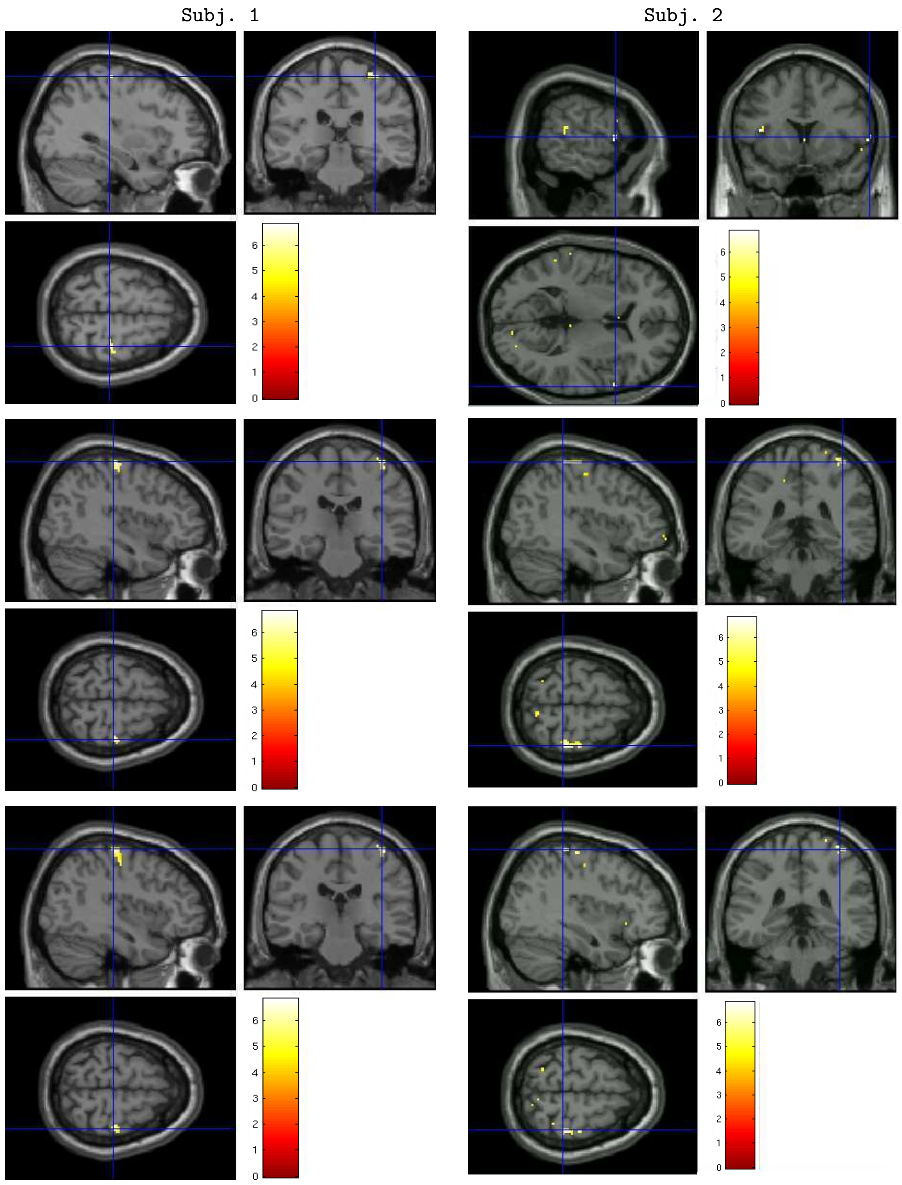

Fig. 8 Between-subject variability of detected activation for the `Lc-Rc` contrast at $R = 4$. Displayed results correspond to `mSENSE` (top row), UWR-SENSE (middle row) and 4D-UWR-SENSE (bottom row). Neurological convention. The blue cross shows the global maximum activation peak.

ones obtained using `mSENSE` and UWR-SENSE, as reported in Tab. 2. Concerning the most significant cluster for $R = 2$, the peak positions remain stable whatever the reconstruction algorithm. However, examining their significance level, one can realize the benefit of wavelet-based regularization when comparing UWR-SENSE with `mSENSE` results and then captures additional positive effects of temporal regularization when looking at the 4D-UWR-SENSE results. These benefits are also demonstrated for $R = 4$.

Table 2 Significant statistical results at the subject-level for the `Ac-As` contrast (corrected for multiple comparisons at $p = 0.05$). Images were reconstructed using the `mSENSE`, UWR-SENSE and 4D-UWR-SENSE algorithm for $R = 2$ and $R = 4$.

		cluster-level		voxel-level		
		p-value	Size	p-value	T-score	Position
$R = 2$	`mSENSE`	$< 10^{-3}$	320	$< 10^{-3}$	6.40	-32 -76 45
		$< 10^{-3}$	163	$< 10^{-3}$	5.96	-4 -70 54
		$< 10^{-3}$	121	$< 10^{-3}$	6.34	34 -74 39
		$< 10^{-3}$	94	$< 10^{-3}$	6.83	-38 4 24
	UWR-SENSE	$< 10^{-3}$	407	$< 10^{-3}$	6.59	-32 -76 45
		$< 10^{-3}$	164	$< 10^{-3}$	5.69	-6 -70 54
		$< 10^{-3}$	159	$< 10^{-3}$	5.84	32 -70 39
		$< 10^{-3}$	155	$< 10^{-3}$	6.87	-44 4 24
	4D-UWR-SENSE	$< 10^{-3}$	**454**	$< 10^{-3}$	6.54	-32 -76 45
		$< 10^{-3}$	199	$< 10^{-3}$	5.43	-6 26 21
		$< 10^{-3}$	183	$< 10^{-3}$	5.89	32 -70 39
		$< 10^{-3}$	170	$< 10^{-3}$	**6.90**	-44 4 24
$R = 4$	`mSENSE`	$< 10^{-3}$	58	0.028	5.16	-30 -72 48
	UWR-SENSE	$< 10^{-3}$	94	0.003	5.91	-32 -70 48
		$< 10^{-3}$	60	0.044	4.42	-6 -72 54
	4D-UWR-SENSE	$< 10^{-3}$	**152**	$< 10^{-3}$	**6.36**	-32 -70 48
		$< 10^{-3}$	36	0.009	5.01	-4 -78 48
		$< 10^{-3}$	29	0.004	5.30	-34 6 27

To summarize, for these two contrasts our 4D-UWR-SENSE algorithm always outperforms the alternative reconstruction methods used in this paper in terms of statistical significance (number of clusters, cluster extent, peak values,...) but also in terms of robustness.

3.2.3 Group-level analysis

Due to between-subject anatomical and functional variability, group-level analysis is necessary in order to derive robust and reproducible conclusions at the population level. For this validation, random effect analyses (RFX) involving fif-

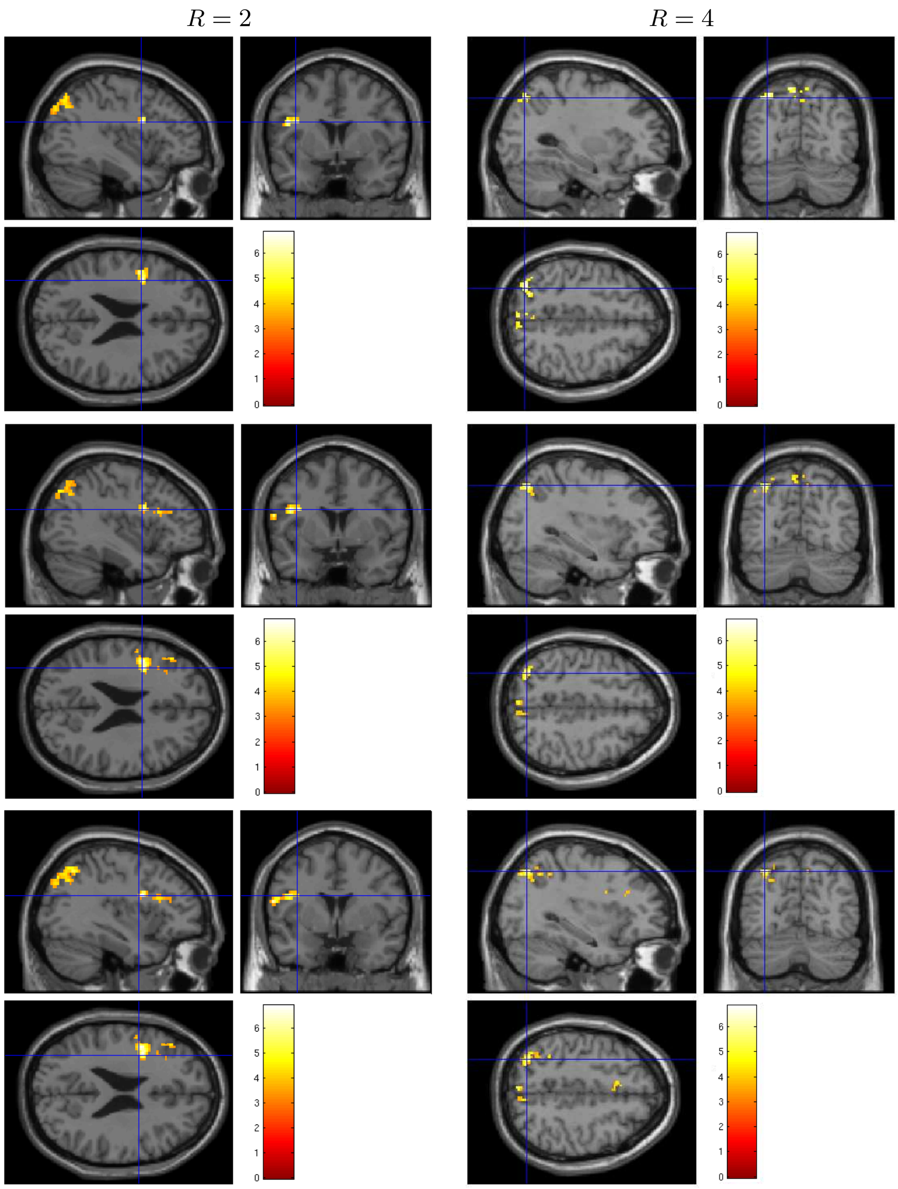

Fig. 9 Student's t-maps superimposed to anatomical MRI for the `Ac-As` contrast. Data have been reconstructed using the `mSENSE` (top row), UWR-SENSE (middle row) and 4D-UWR-SENSE (bottom row). Neurological convention: **left is left**. The blue cross shows the global maximum activation peak.

teen healthy subjects have been conducted on the contrast maps we previously investigated at the subject level. More precisely, one-sample Student's t test was performed on the subject-level contrast images (eg, `Lc-Rc`, `Ac-As`,... images) using SPM5.

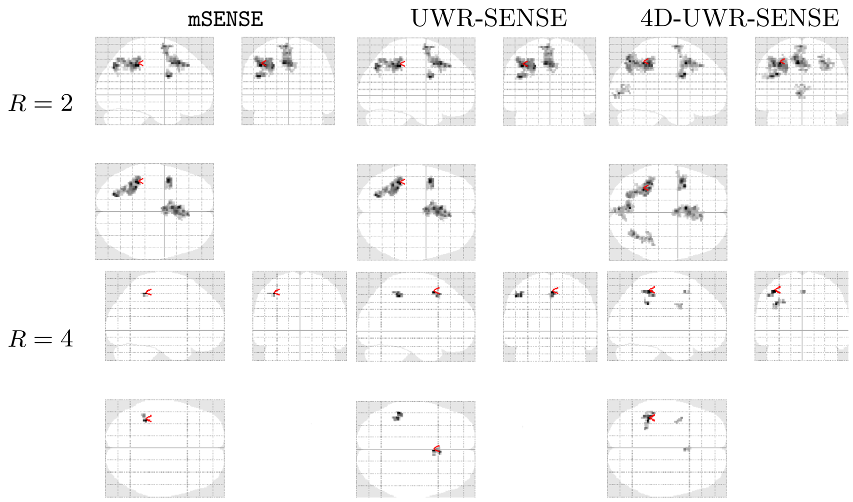

Fig. 10 Group-level Student's t-maps for the `Ac-As` contrast where data have been reconstructed using the `mSENSE`, UWR-SENSE and 4D-UWR-SENSE for $R = 2$ and $R = 4$. Neurological convention. Red arrows indicate the global maximum activation peak.

For the `Ac-As` contrast, Maximum Intensity Projection (MIP) Student's t-maps are shown in Fig. 10. First, they illustrate that irrespective of the reconstruction method larger and more significant activations are found on datasets acquired with $R = 2$ providing the better SNR. Second, for $R = 2$, visual inspection of Fig. 10 [top] confirms that only the 4D-UWR-SENSE algorithm allows us to retrieve significant bilateral activations in the parietal cortices (see axial MIP slices) in addition to larger cluster extent and a gain in significance level for the stable clusters across the different reconstructors. Similar conclusions can be drawn when looking at Fig. 10 [bottom] for $R = 4$. Complementary results are available in Tab. 3 for $R = 2$ and $R = 4$. These results allow us to numerically validate this visual comparison:

Table 3 Significant statistical results at the group-level for the `Ac-As` contrast (corrected for multiple comparisons at $p = 0.05$). Images were reconstructed using the `mSENSE`, UWR-SENSE and 4D-UWR-SENSE algorithms for $R = 2$ and $R = 4$.

		cluster-level		voxel-level		
		p-value	Size	p-value	T-score	Position
$R = 2$	`mSENSE`	$< 10^{-3}$	361	0.014	7.68	-6 -22 45
		$< 10^{-3}$	331	0.014	8.23	-40 -38 42
		$< 10^{-3}$	70	0.014	7.84	-44 6 27
	UWR-SENSE	$< 10^{-3}$	361	0.014	7.68	-6 22 45
		$< 10^{-3}$	331	0.014	7.68	-44 -38 42
		$< 10^{-3}$	70	0.014	7.84	-44 6 27
	4D-UWR-SENSE	$< 10^{-3}$	**441**	$< 10^{-3}$	**9.45**	-32 -50 45
		$< 10^{-3}$	338	$< 10^{-3}$	9.37	-6 12 45
		$< 10^{-3}$	152	0.010	7.19	30 -64 48
$R = 4$	`mSENSE`	0.003	14	0.737	5.13	-38 -42 51
	UWR-SENSE	$< 10^{-3}$	**41**	0.274	5.78	-50 -38 -48
		$< 10^{-3}$	32	0.274	5.91	2 12 54
	4D-UWR-SENSE	$< 10^{-3}$	37	0.268	**6.46**	-40 -40 54
		$< 10^{-3}$	25	0.268	6.37	-38 -42 36
		$< 10^{-3}$	18	0.273	5	-42 8 36

– Whatever the reconstruction method in use, the statistical performance is much more significant using $R = 2$, especially at the cluster level since the cluster extent decreases by one order of magnitude.
– Voxel and cluster-level results are enhanced using the 4D-UWR-SENSE approach instead of the `mSENSE` reconstruction or its early UWR-SENSE version.

Fig. 11 reports similar group-level MIP results for $R = 2$ and $R = 4$ concerning the `Lc-Rc` contrast. It is shown that whatever the acceleration factor R in use, our pipeline enables to detect a much more spatially extended activation area in the motor cortex. This visual inspection is quantitatively confirmed in Tab. 4 when comparing the detected clusters using our 4D-UWR-SENSE approach with those found by `mSENSE`, again irrespective of R. Finally, the 4D-UWR-SENSE algorithm outperforms the UWR-SENSE one, which corroborates the benefits of the proposed spatio-temporal regularization scheme.

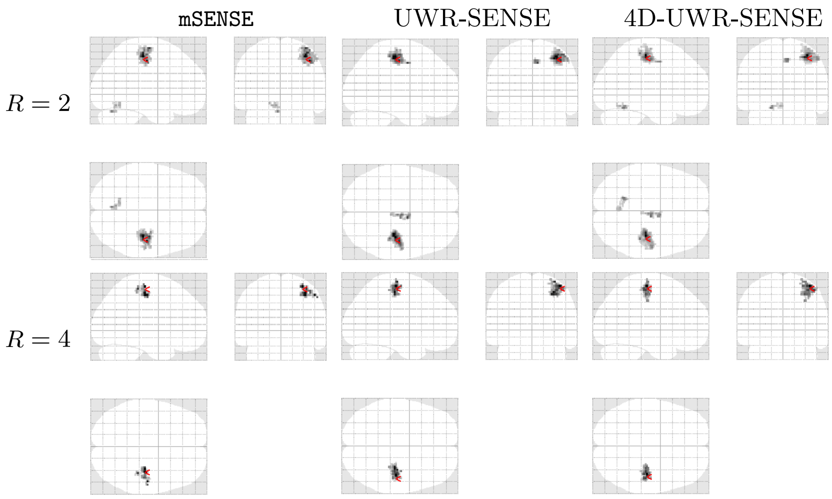

Fig. 11 Group-level Student's t-maps for the `Lc-Rc` contrast where data have been reconstructed using the `mSENSE`, UWR-SENSE and 4D-UWR-SENSE for $R = 2$ and $R = 4$. Neurological convention. Red arrows indicate the global maximum activation peak.

Table 4 Significant statistical results at the group-level for the `Lc-Rc` contrast (corrected for multiple comparisons at $p = 0.05$). Images were reconstructed using the `mSENSE`, UWR-SENSE and 4D-UWR-SENSE algorithms for $R = 2$ and $R = 4$.

		cluster-level		voxel-level		
		p-value	Size	p-value	T-score	Position
$R = 2$	`mSENSE`	$< 10^{-3}$	354	$< 10^{-3}$	9.48	38 -22 54
		0.001	44	0.665	6.09	-4 -68 -24
	UWR-SENSE	$< 10^{-3}$	350	0.005	9.83	36 -22 57
		$< 10^{-3}$	35	0.286	7.02	4 -12 51
	4D-UWR-SENSE	$< 10^{-3}$	**377**	0.001	**11.34**	36 -22 57
		$< 10^{-3}$	53	$< 10^{-3}$	7.50	8 -14 51
		$< 10^{-3}$	47	$< 10^{-3}$	7.24	-18 -54 -18
$R = 4$	`mSENSE`	$< 10^{-3}$	38	0.990	5.97	32 -20 45
	UWR-SENSE	$< 10^{-3}$	163	0.128	7.51	46 -18 60
	4D-UWR-SENSE	$< 10^{-3}$	**180**	0.111	**7.61**	46 -18 60

4 Discussion

Through illustrated results, we showed that whole brain acquisition can be routinely used at a spatial in-plane resolution of 2×2 mm^2 in a short and constant repetition time (TR = 2.4 s) provided that a reliable pMRI reconstruction pipeline is chosen. In this paper, we demonstrated that our 4D-UWR-SENSE reconstruction algorithm meets this goal. To draw this conclusion, qualitative comparisons have been made directly on reconstructed images using our pipeline involving the

3D and 4D-UWR-SENSE algorithms or mSENSE. On anatomical data where the acquisition scheme is fully 3D, our results confirm the usefulness of the 3D wavelet regularization for attenuating 3D spatially propagating artifacts. However, as usually observed in the wavelet restoration literature, we can notice the presence of slight motion-like artifacts in the reconstructed image background. Compared to mSENSE images, our method provides lower contrast level, which is actually not a drawback since the improved contrast in mSENSE images is the result of post-processings embedded in the reconstruction pipeline of the scanner manufacturer. Functional data results show that, even when the acquisition scheme is 2D sequential, reconstruction artifacts are attenuated by resorting simultaneously to the 3D wavelet and temporal regularizations. In the case of interleaved 2D acquisition scheme where contiguous slices are acquired every TR/2, motion artifacts may dramatically alter the reconstruction quality using the mSENSE method. Although the actual version of the proposed algorithm does not account for such artifacts, a trade-off between the two regularizers may be found to cope with this issue.

Quantitatively speaking, our comparison took place at the statistical analysis level and relied on quantitative criteria (voxel- and cluster-level corrected p-values, t-scores, peak positions) at the subject and group levels. In particular, we showed that our 4D-UWR-SENSE approach outperforms both its UWR-SENSE ancestor [37] and the mSENSE reconstruction [17] in terms of statistical significance and robustness. This emphasized the benefits of combining temporal and 3D wavelet-based regularization. The usefulness of 3D regularization in reconstructing 3D anatomical images was also shown, especially in more degraded situations ($R = 4$) where regularization plays a prominent role. The validity of our conclusions lies in the reasonable size of our datasets: the same 15 participants were scanned using two different pMRI acceleration factors ($R = 2$ and $R = 4$).

At the considered spatio-temporal compromise ($2 \times 2 \times 3$ mm^3 and TR $= 2.4$ s), we also illustrated the impact of increasing the acceleration factor (passing from $R = 2$ to $R = 4$) on the statistical sensitivity at the subject and group levels for a given reconstruction algorithm. We performed this comparison to anticipate what could be the statistical performance for detecting evoked brain activity on data requiring this acceleration factor, such as high spatial resolution EPI images (e.g., 1.5×1.5 mm^2 in-plane resolution) acquired in the same short TR. Our conclusions were balanced depending on the contrast of interest: when looking at the `Ac-As` contrast involving the fronto-parietal network, it turned out that $R = 4$ was not reliable enough to recover significant group-level activity at 3 Tesla: the SNR loss was too important and should be compensated by an increase of the static magnetic field (e.g. passing from 3 to 7 Tesla). However, the situation becomes acceptable for the `Lc-Rc` motor contrast, which elicits activation in motor regions: our results brought evidence that the 4D-UWR-SENSE approach enables the use of $R = 4$ for this contrast.

5 Conclusion

Two main contributions have been developed. First, we proposed a novel reconstruction method that relies on a 3D wavelet transform and accounts for temporal dependencies in successive fMRI volumes. As a particular case, the proposed method allows us to deal with 3D acquired anatomical data when a single volume is acquired. Second, when artifacts were superimposed to brain activation, we showed that the choice of the pMRI reconstruction algorithm has a significant influence on the statistical sensitivity in fMRI and may enable whole brain neuroscience studies at high spatial resolution. Our results brought evidence that the compromise between acceleration factor and spatial in-plane resolution should be selected with care depending on the regions involved in the fMRI paradigm. As a consequence, high resolution fMRI studies can be conducted using high speed acquisition (short TR and large R value) provided that the expected BOLD effect is strong, as experienced in primary motor, visual and auditory cortices.

A direct extension of the present work consists of studying the impact of tight frames instead of wavelet bases to define more suitable 3D transforms. However, unsupervised reconstruction becomes more challenging in this framework since the estimation of hyper-parameters becomes cumbersome (see [59] for details). Integrating some pre-processing steps in the reconstruction model may also be of great interest to account for motion artifacts in the regularization step, especially for interleaved 2D acquisition schemes. Such an extension deserves integration of recent works on joint correction of motion and slice-timing such as [60]. Another extension of our work would concern the combination of our wavelet-regularized reconstruction with the WSPM approach [64] in which statistical analysis is directly performed in the wavelet transform domain.

Appendix

A Optimization procedure for the 4D reconstruction

The minimization of $\mathcal{J}_{\rm ST}$ in Eq. (8) is performed by resorting to the concept of proximity operators [65], which was found to be fruitful in a number of recent works in convex optimization [66, 67, 68]. In what follows, we recall the definition of a proximity operator.

Definition 1 [65] Let $\Gamma_0(\chi)$ be the class of proper lower semicontinuous convex functions from a separable real Hilbert space χ to $]-\infty,+\infty]$ and let $\varphi \in \Gamma_0(\chi)$. For every $\mathrm{x} \in \chi$, the function $\varphi + \|\cdot - \mathrm{x}\|^2/2$ achieves its infimum at a unique point denoted by $\mathrm{prox}_\varphi \mathrm{x}$. The operator $\mathrm{prox}_\varphi \,:\, \chi \to \chi$ is the proximity operator of φ.

In this work, as the observed data are complex-valued, the definition of proximity operators is extended to a class of convex functions defined for complex-valued variables. For the function

$$\begin{aligned} \Phi\colon \mathbb{C}^K &\to]-\infty,+\infty] \\ x &\mapsto \phi^{\rm Re}(\mathrm{Re}(x)) + \phi^{\rm Im}(\mathrm{Im}(x)), \end{aligned} \tag{12}$$

where $\phi^{\rm Re}$ and $\phi^{\rm Im}$ are functions in $\Gamma_0(\mathbb{R}^K)$ and $\mathrm{Re}(x)$ (respectively $\mathrm{Im}(x)$) is the vector of the real parts (respectively imaginary parts) of the components of $x \in \mathbb{C}^K$, the proximity operator is defined as

$$\begin{aligned} \mathrm{prox}_\Phi\colon \mathbb{C}^K &\to \mathbb{C}^K \\ x &\mapsto \mathrm{prox}_{\phi^{\rm Re}}(\mathrm{Re}(x)) + \imath\,\mathrm{prox}_{\phi^{\rm Im}}(\mathrm{Im}(x)). \end{aligned} \tag{13}$$

Let us now provide the expressions of proximity operators involved in our reconstruction problem.

A.1 Proximity operator of the data fidelity term

According to standard rules on the calculation of proximity operators [68, Table 1.1] while denoting $\rho^t = T^*\zeta^t$, the proximity operator of the data fidelity term $\mathcal{J}_{\mathrm{WLS}}$ is given for every vector of coefficients ζ^t (with $t \in \{1,\ldots,N_r\}$) by $\mathrm{prox}_{\mathcal{J}_{\mathrm{WLS}}}(\zeta^t) = Tu^t$, where the image u^t is such that $\forall \mathbf{r} \in \{1,\ldots,X\} \times \{1,\ldots,Y/R\} \times \{1,\ldots,Z\}$,

$$\boldsymbol{u}^t(\mathbf{r}) = \big(\boldsymbol{I}_R + 2\boldsymbol{S}^{\mathsf{H}}(\mathbf{r})\boldsymbol{\Psi}^{-1}\boldsymbol{S}(\mathbf{r})\big)^{-1}\big(\boldsymbol{\rho}^t(\mathbf{r}) + 2\boldsymbol{S}^{\mathsf{H}}(\mathbf{r})\boldsymbol{\Psi}^{-1}\boldsymbol{d}^t(\mathbf{r})\big). \tag{14}$$

A.2 Proximity operator of the spatial regularization function

According to [37], for every resolution level j and orientation o, the proximity operator of the spatial regularization function $\Phi_{o,j}$ is given by

$$\forall \xi \in \mathbb{C}, \qquad \mathrm{prox}_{\Phi_{o,j}}\xi = \frac{\mathrm{sign}(\mathrm{Re}(\xi - \mu_{o,j}))}{\beta^{\mathrm{Re}}_{o,j}+1}\max\{|\mathrm{Re}(\xi-\mu_{o,j})| - \alpha^{\mathrm{Re}}_{o,j}, 0\} + \imath\frac{\mathrm{sign}(\mathrm{Im}(\xi - \mu_{o,j}))}{\beta^{\mathrm{Im}}_{o,j}+1}\max\{|\mathrm{Im}(\xi-\mu_{o,j})| - \alpha^{\mathrm{Im}}_{o,j}, 0\} + \mu_{o,j} \tag{15}$$

where the sign function is defined as follows:

$$\forall \xi \in \mathbb{R}, \qquad \mathrm{sign}(\xi) = \begin{cases} +1 & \text{if } \xi \geq 0 \\ -1 & \text{otherwise.} \end{cases}$$

A.3 Proximity operator of the temporal regularization function

A simple expression of the proximity operator of function h is not available. We thus propose to split this regularization term as a sum of two more tractable functions h_1 and h_2:

$$h_1(\zeta) = \kappa \sum_{t=1}^{N_r/2} \|T^*\zeta^{2t} - T^*\zeta^{2t-1}\|_p^p \tag{16}$$

$$h_2(\zeta) = \kappa \sum_{t=1}^{N_r/2-1} \|T^*\zeta^{2t+1} - T^*\zeta^{2t}\|_p^p. \tag{17}$$

Since h_1 (respectively h_2) is separable w.r.t the time variable t, its proximity operator can easily be calculated based on the proximity operator of each of the involved terms in the sum of Eq. (16) (respectively Eq. (17)). Indeed, let us consider the following function

$$\begin{aligned} \Psi : \mathbb{C}^K \times \mathbb{C}^K &\longrightarrow \mathbb{R} \\ (\zeta^t, \zeta^{t-1}) &\mapsto \kappa \| T^* \zeta^t - T^* \zeta^{t-1} \|_p^p = \psi \circ H(\zeta^t, \zeta^{t-1}), \end{aligned} \tag{18}$$

where $\psi = \kappa \| T^* \cdot \|_p^p$ and H is the linear operator defined as

$$\begin{aligned} H : \mathbb{C}^K \times \mathbb{C}^K &\longrightarrow \mathbb{C}^K \\ (a, b) &\mapsto a - b. \end{aligned} \tag{19}$$

Its associated adjoint operator H^* is therefore given by

$$\begin{aligned} H^* : \mathbb{C}^K &\longrightarrow \mathbb{C}^K \times \mathbb{C}^K \\ a &\mapsto (a, -a). \end{aligned} \tag{20}$$

Since $HH^* = 2\mathrm{Id}$, the proximity operator of Ψ can easily be calculated using [69, Prop. 11]:

$$\mathrm{prox}_{\Psi} = \mathrm{prox}_{\psi \circ H} = \mathrm{Id} + \frac{1}{2} H^* \circ (\mathrm{prox}_{2\psi} - \mathrm{Id}) \circ H. \tag{21}$$

The calculation of $\mathrm{prox}_{2\psi}$ is discussed in [66].

A.4 Parallel Proximal Algorithm (PPXA)

The function to be minimized has been reexpressed as

$$\begin{aligned} \mathcal{J}_{\mathrm{ST}}(\zeta) = &\sum_{t=1}^{N_r} \sum_{\mathbf{r} \in \{1,\ldots,X\} \times \{1,\ldots,Y/R\} \times \{1,\ldots,Z\}} \| \boldsymbol{d}^t(\boldsymbol{r}) - \boldsymbol{S}(\boldsymbol{r})(T^* \zeta^t)(\boldsymbol{r}) \|_{\boldsymbol{\Psi}^{-1}}^2 \\ &+ g(\zeta) + h_1(\zeta) + h_2(\zeta). \end{aligned} \tag{22}$$

Since $\mathcal{J}_{\mathrm{ST}}$ is made up of more than two non-necessarily differentiable terms, an appropriate solution for minimizing such an optimality criterion is PPXA [47]. In particular, it is important to note that this algorithm does not require subiterations as was the case for the constrained optimization algorithm proposed in [37]. In addition, the computations in this algorithm can be performed in a parallel manner and the convergence of the algorithm to an optimal solution to the minimization problem is guaranteed.

The resulting algorithm for the minimization of the optimality criterion in Eq. (22) is given in Algorithm 1. In this algorithm, the weights ω_i have been fixed to 1/4 for every $i \in \{1, \ldots, 4\}$. The parameter γ has been set to 200 since this value was observed to lead to the fastest convergence in practice. The stopping parameter ε has been set to 10^{-4}. Using these parameters, the algorithm typically converges in less than 50 iterations.

Algorithm 1 4D-UWR-SENSE: spatio-temporal regularized reconstruction.

Set $\gamma \in]0, +\infty[$, $\varepsilon \in]0, 1[$, $(\omega_i)_{1 \le i \le 4} \in]0, 1[^4$ such that $\sum_{i=1}^4 \omega_i = 1$, $n = 0$, $(\zeta_i^{(n)})_{1 \le i \le 4} \in (\mathbb{C}^{K \times N_r})^4$ where $\zeta_i^{(n)} = (\zeta_i^{1,(n)}, \zeta_i^{2,(n)}, \ldots, \zeta_i^{N_r,(n)})$, and $\zeta_i^{t,(n)} = \big((\boldsymbol{\zeta}_{i,a}^{t,(n)}), ((\boldsymbol{\zeta}_{i,o,j}^{t,(n)}))_{o \in \mathbb{O}, 1 \le j \le j_{\max}}\big)$ for every $i \in \{1, \ldots, 4\}$ and $t \in \{1, \ldots, N_r\}$. Set also $\zeta^{(n)} = \sum_{i=1}^4 \omega_i \zeta_i^{(n)}$ and $\mathcal{J}_{\mathrm{ST}}^{(n)} = 0$.

repeat
  Set $p_4^{1,(n)} = \zeta_4^{1,(n)}$.
  for $t = 1$ to N_r **do**
    Compute $p_1^{t,(n)} = \mathrm{prox}_{\gamma \mathcal{J}_{\mathrm{WLS}}/\omega_1}(\zeta_1^{t,(n)})$.
    Compute $p_2^{t,(n)} = \big(\mathrm{prox}_{\gamma \Phi_a/\omega_2}(\boldsymbol{\zeta}_{2,a}^{t,(n)}), (\mathrm{prox}_{\gamma \Phi_{o,j}/\omega_2}(\boldsymbol{\zeta}_{2,o,j}^{t,(n)}))_{o \in \mathbb{O}, 1 \le j \le j_{\max}}\big)$.
    if t is even **then**
      Compute $(p_3^{t,(n)}, p_3^{t-1,(n)}) = \mathrm{prox}_{\gamma \Psi/\omega_3}(\zeta_3^{t,(n)}, \zeta_3^{t-1,(n)})$
    else if t is odd and $t > 1$ **then**
      Compute $(p_4^{t,(n)}, p_4^{t-1,(n)}) = \mathrm{prox}_{\gamma \Psi/\omega_4}(\zeta_4^{t,(n)}, \zeta_4^{t-1,(n)})$.
    end if
    if $t > 1$ **then**
      Set $P^{t-1,(n)} = \sum_{i=1}^4 \omega_i p_i^{t-1,(n)}$.
    end if
  end for
  Set $p_4^{N_r,(n)} = \zeta_4^{N_r,(n)}$.
  Compute $P^{N_r,(n)} = \sum_{i=1}^4 \omega_i p_i^{N_r,(n)}$.
  Set $P^{(n)} = (P^{1,(n)}, P^{2,(n)}, \ldots, P^{N_r,(n)})$.
  Set $\lambda_n \in [0, 2]$.
  for $i = 1$ to 4 **do**
    Set $p_i^{(n)} = (p_i^{1,(n)}, p_i^{2,(n)}, \ldots, p_i^{N_r,(n)})$.
    Compute $\zeta_i^{(n)} = \zeta_i^{(n)} + \lambda_n (2P^{(n)} - \zeta^{(n)} - p_i^{(n)})$.
  end for
  Compute $\zeta^{(n+1)} = \zeta^{(n)} + \lambda_n (P^{(n)} - \zeta^{(n)})$.
  $n \leftarrow n + 1$.
until $|\mathcal{J}_{\mathrm{ST}}(\zeta^{(n)}) - \mathcal{J}_{\mathrm{ST}}(\zeta^{(n-1)})| \le \varepsilon \mathcal{J}_{\mathrm{ST}}(\zeta^{(n-1)})$.
Set $\hat{\zeta} = \zeta^{(n)}$.
return $\hat{\rho}^t = T^* \hat{\zeta}^t$ for every $t \in \{1, \ldots, N_r\}$.

References

1. Chaari L, Mériaux S, Badillo S, Ciuciu P, Pesquet JC (2011) 3D wavelet-based regularization for parallel MRI reconstruction: impact on subject and group-level statistical sensitivity

in fMRI. In: In IEEE International Sympsium on Biomedical Imaging (ISBI), Chicago, USA, pp 460–464

2. Kochunov P, Rivière D, Lancaster JL, Mangin JF, Cointepas Y, Glahn D, Fox P, Rogers J (2005) Development of high-resolution MRI imaging and image processing for live and post-mortem primates. In: Hum. Brain Mapp., Toronto, Canada, vol 26 (1)
3. Rabrait C, Ciuciu P, Ribès A, Poupon C, Leroux P, Lebon V, Dehaene-Lambertz G, Bihan DL, Lethimonnier F (2008) High temporal resolution functional MRI using parallel echo volume imaging. Magn Reson Imag 27(4):744–753
4. Sodickson DK, Manning WJ (1997) Simultaneous acquisition of spatial harmonics (SMASH): fast imaging with radiofrequency coil arrays. Magn Reson in Med 38(4):591–603
5. Pruessmann KP, Weiger M, Scheidegger MB, Boesiger P (1999) SENSE: sensitivity encoding for fast MRI. Magn Reson in Med 42(5):952–962
6. Griswold MA, Jakob PM, Heidemann RM, Nittka M, Jellus V, Wang J, Kiefer B, Haase A (2002) Generalized autocalibrating partially parallel acquisitions GRAPPA. Magn Reson in Med 47(6):1202–1210
7. Candès E, Romberg J, Tao T (2006) Robust uncertainty principles: exact signal reconstruction from highly incomplete frequency information. IEEE Trans Inf Theory 52(2):489–509
8. Lustig M, Donoho D, Pauly JM (2007) Sparse MRI: The application of compressed sensing for rapid MR imaging. Magn Reson in Med 58:1182–1195
9. Bilgin A, Trouard T P, Gmitro A F, Altbach M. I (2008) Randomly Perturbed Radial Trajectories for Compressed Sensing MRI. In: Meeting of the International Society for Magnetic Resonance in Medicine, Toronto, Canada
10. Yang A, Feng L, Xu J, Selesnick I, Sodickson D K, Otazo R (2012) Improved Compressed Sensing Reconstruction with Overcomplete Wavelet Transforms. In: Meeting of the International Society for Magnetic Resonance in Medicine, Melbourne, Australia
11. Holland D J, Liu C, Song X, Mazerolle E L, Stevens M T, Sederman A J, Gladden L F, D'Arcy R C N, Bowen C V, Beyea S D (2013) Compressed sensing reconstruction improves sensitivity of variable density spiral fMRI. Magn Reson in Med doi: 10.1002/mrm.24621
12. Liang D, Liu B, Wang J, Ying L (2009) Accelerating SENSE using compressed sensing. Magn Reson in Med 62(6):1574–84
13. Boyer C, Ciuciu P, Weiss P, Mériaux S (2012) HYR^{2}PICS: Hybrid regularized reconstruction for combined parallel imaging and compressive sensing in MRI. In: 9th International Symposium on Biomedical Imaging (ISBI), Barcelona, Spain, pp 66–69
14. Madore B, Glover GH, Pelc NJ (1999) Unaliasing by Fourier-encoding the overlaps using the temporal dimension (UNFOLD), applied to cardiac imaging and fMRI. Magn Reson in Med 42(5):813–28

15. Tsao J, Boesiger P, Pruessmann KP (2003) k-t BLAST and k-t SENSE: dynamic MRI with high frame rate exploiting spatiotemporal correlations. Magn Reson in Med 50(5):1031–42
16. Lustig M., Santos J.M., Donoho D.L., Pauly J.M (2001) k-t SPARSE: High Frame Rate Dynamic MRI Exploiting Spatio-Temporal Sparsity. In: International Society for Magnetic Resonance in Medicine, Washington, USA, 1p.
17. Wang J, Kluge T, Nittka M, Jellus V, Kuhn B, Kiefer B (2001) Parallel acquisition techniques with modified SENSE reconstruction mSENSE. In: 1st Wuzburg Workshop on Parallel Imaging Basics and Clinical Applications, Wuzburg, Germany, 1p.
18. Tsao J, Kozerke S, Boesiger P, Pruessmann KP (2005) Optimizing spatiotemporal sampling for k-t BLAST and k-t SENSE: application to high-resolution real-time cardiac steady-state free precession. Magn Reson in Med 53(6):1372–82
19. Huang F, Akao J, Vijayakumar S, Duensing GR, Limkeman M (2005) k-t GRAPPA: a k-space implementation for dynamic MRI with high reduction factor. Magn Reson in Med 54(5):1172–84
20. Jung H, Ye JC, Kim EY (2007) Improved k-t BLAST and k-t SENSE using FOCUSS. Phys in Med and Biol 52(11):3201–26
21. Jung H, Sung K, Nayak KS, Kim EY, Ye JC (2009) k-t FOCUSS: a general compressed sensing framework for high resolution dynamic MRI. Magn Reson in Med 61(1):103–16
22. Damoiseaux JS, Rombouts SA, Barkhof F, Scheltens P, Stam CJ, Smith SM, Beckmann CF (2006) Consistent resting-state networks across healthy subjects. Proc Natl Acad Sci USA 103(37):13,848–13,853
23. Dale AM (1999) Optimal experimental design for event-related fMRI. Hum Brain Mapp 8:109–114
24. Varoquaux G, Sadaghiani S, Pinel P, Kleinschmidt A, Poline JB, Thirion B (2010) A group model for stable multi-subject ICA on fMRI datasets. Neuroimage 51(1):288–299
25. Ciuciu P, Varoquaux G, Abry P, Sadaghiani S, Kleinschmidt A (2012) Scale-free and multifractal time dynamics of fMRI signals during rest and task. Frontiers in physiology 3(Article 186):1–18
26. Birn R, Cox R, Bandettini PA (2002) Detection versus estimation in event-related fMRI: choosing the optimal stimulus timing. Neuroimage 15(1):252–264
27. Logothetis NK (2008) What we can do and what we cannot do with fMRI. Nature 453(7197):869–878
28. de Zwart J, Gelderen PV, Kellman P, Duyn JH (2002) Application of sensitivity-encoded echo-planar imaging for blood oxygen level-dependent functional brain imaging. Magn Reson in Med 48(6):1011–20

29. Preibisch C (2003) Functional MRI using sensitivity-encoded echo planar imaging (SENSE-EPI). Neuroimage 19(2):412–421
30. de Zwart J, Gelderen PV, Golay X, Ikonomidou VN, Duyn JH (2006) Accelerated parallel imaging for functional imaging of the human brain. NMR Biomed 19(3):342–51
31. Utting JF, Kozerke S, Schnitker R, Niendorf T (2010) Comparison of k-t SENSE/k-t BLAST with conventional SENSE applied to BOLD fMRI. J of Magn Reson Imag 32(1):235–41
32. Liang ZP, Bammer R, Ji J, Pelc NJ, Glover GH (2002) Making better SENSE: wavelet denoising, Tikhonov regularization, and total least squares. In: International Society for Magnetic Resonance in Medicine, Hawaï, USA, p 2388
33. Ying L, Xu D, Liang ZP (2004) On Tikhonov regularization for image reconstruction in parallel MRI. In: IEEE Engineering in Medicine and Biology Society, San Francisco, USA, pp 1056–1059
34. Zou YM, Ying L, Liu B (2008) SparseSENSE: application of compressed sensing in parallel MRI. In: IEEE International Conference on Technology and Applications in Biomedicine, Shenzhen, China, pp 127–130
35. Chaari L, Pesquet JC, Benazza-Benyahia A, Ciuciu P (2008) Autocalibrated parallel MRI reconstruction in the wavelet domain. In: IEEE International Symposium on Biomedical Imaging (ISBI), Paris, France, pp 756–759
36. Liu B, Abdelsalam E, Sheng J, , Ying L (2008) Improved spiral SENSE reconstruction using a multiscale wavelet model. In: IEEE International Symposium on Biomedical Imaging (ISBI), Paris, France, pp 1505–1508
37. Chaari L, Pesquet JC, Benazza-Benyahia A, Ciuciu P (2011) A wavelet-based regularized reconstruction algorithm for SENSE parallel MRI with applications to neuroimaging. Med Image Anal 15(2):185–2010
38. Chaari L, Mériaux S, Pesquet JC, Ciuciu P (2010) Impact of the parallel imaging reconstruction algorithm on brain activity detection in fMRI. In: International Symposium on Applied Sciences in Biomedical and Communication Technologies (ISABEL), Rome, Italy
39. Jakob P, Griswold M, Breuer F, Blaimer M, Seiberlich N (2006) A 3D GRAPPA algorithm for volumetric parallel imaging. In: Scientific Meeting International Society for Magnetic Resonance in Mededicine, Seattle, USA, p 286
40. Aguirre GK, Zarahn E, D'Esposito M (1997) Empirical analysis of BOLD fMRI statistics. II. Spatially smoothed data collected under null-hypothesis and experimental conditions. Neuroimage 5(3):199–212
41. Zarahn E, Aguirre GK, D'Esposito M (1997) Empirical analysis of BOLD fMRI statistics. I. Spatially unsmoothed data collected under null-hypothesis conditions. Neuroimage

5(3):179–197

42. Purdon PL, Weisskoff RM (1998) Effect of temporal autocorrelation due to physiological noise and stimulus paradigm on voxel-level false-positive rates in fMRI. Hum Brain Mapp 6(4):239–249
43. Woolrich M, Ripley B, Brady M, Smith S (2001) Temporal autocorrelation in univariate linear modelling of fMRI data. Neuroimage 14(6):1370–1386
44. Worsley KJ, Liao CH, Aston J, Petre V, Duncan GH, Morales F, Evans AC (2002) A general statistical analysis for fMRI data. Neuroimage 15(1):1–15
45. Penny WD, Kiebel S, Friston KJ (2003) Variational Bayesian inference for fMRI time series. Neuroimage 19(3):727–741
46. Chaari L, Vincent T, Forbes F, Dojat M, Ciuciu P (2013) Fast joint detection-estimation of evoked brain activity in event-related fMRI using a variational approach. IEEE Trans on Med Imag 32(5):821–837
47. Combettes PL, Pesquet JC (2008) A proximal decomposition method for solving convex variational inverse problems. Inverse Problems 24(6):27
48. Guerquin-Kern M, Haberlin M, Pruessmann KP, Unser M (2011) A fast wavelet-based reconstruction method for magnetic resonance imaging. IEEE Trans on Med Imaging 30(9):1649–1660
49. Sodickson DK (2000) Tailored SMASH image reconstructions for robust in vivo parallel MR imaging. Magn Reson in Med 44(2):243251
50. Rowe D. B. (2005) Modeling both the magnitude and phase of complex-valued fMRI data. Neuroimage 25:1310–1324
51. Keeling SL (2003) Total variation based convex filters for medical imaging. Appl Math and Comput 139(1):101–1195
52. Liu B, King K, Steckner M, Xie J, Sheng J, Ying L (2008) Regularized sensitivity encoding (SENSE) reconstruction using Bregman iterations. Magn Reson in Med 61(1):145 – 152
53. Sümbül U, Santos JM, Pauly JM (2009) Improved time series reconstruction for dynamic magnetic resonance imaging. IEEE Trans on Med Imag 28(7):1093–1104
54. Pinel P, Thirion B, Mériaux S, Jobert A, Serres J, Le Bihan D, Poline JB, Dehaene S (2007) Fast reproducible identification and large-scale databasing of individual functional cognitive networks. BMC Neuroscience 8(1):91
55. Daubechies I (1992) Ten Lectures on Wavelets. Society for Industrial and Applied Mathematics, Philadelphia
56. Dehaene S (1999) Cerebral bases of number processing and calculation. In: Gazzaniga M (ed) The New Cognitive Neurosciences, MIT Press, Cambridge,, chap 68, pp 987–998

57. Nichols TE, Hayasaka S (2003) Controlling the Familywise Error Rate in Functional Neuroimaging: A Comparative Review. Stat Methods in Med Res 12(5):419–446
58. Brett M, Penny W, Kiebel S (2004) Introduction to random field theory. In: Frackowiak RSJ, Friston KJ, Fritch CD, Dolan RJ, Price CJ, Penny WD (eds) Hum. Brain Funct., 2nd edn, Academic Press, pp 867–880
59. Chaari L, Pesquet JC, Tourneret JY, Ciuciu P, Benazza-Benyahia A (2010) A hierarchical Bayesian model for frame representation. IEEE Trans on Signal Process (11):5560–5571
60. Roche A (2011) A four-dimensional registration algorithm with application to joint correction of motion and slice timing in fMRI. IEEE Trans on Med Imag 30(8):1546–1554
61. Makni S, Idier J, Vincent T, Thirion B, Dehaene-Lambertz G, Ciuciu P (2008) A fully Bayesian approach to the parcel-based detection-estimation of brain activity in fMRI. Neuroimage 41(3):941–969
62. Vincent T, Risser L, Ciuciu P (2010) Spatially adaptive mixture modeling for analysis of within-subject fMRI time series. IEEE Trans on Med Imag 29(4):1059–1074
63. Badillo S, Vincent T, Ciuciu P (2013) Group-level impacts of within- and between-subject hemodynamic variability in fMRI. Neuroimage 82:433–448
64. Van De Ville D, Seghier M, Lazeyras F, Blu T, Unser M (2007) WSPM: Wavelet-based statistical parametric mapping. Neuroimage 37(4):1205–1217
65. Moreau JJ (1965) Proximité et dualité dans un espace hilbertien. Bull de la Société Math de Fr 93:273–299
66. Chaux C, Combettes P, Pesquet JC, Wajs VR (2007) A variational formulation for frame-based inverse problems. Inverse Problems 23(4):1495–1518
67. Combettes PL, Wajs VR (2005) Signal recovery by proximal forward-backward splitting. Multiscale Model and Simul 4:1168–1200
68. Combettes PL, Pesquet JC (2010) Proximal splitting methods in signal processing. In: Bauschke HH, Burachik R, Combettes PL, Elser V, Luke DR, Wolkowicz H (eds) Fixed-Point Algorithms for Inverse Problems in Science and Engineering, Springer Verlag, New York, chap 1, pp 185–212
69. Combettes PL, Pesquet JC (2007) A Douglas-Rachford splitting approach to nonsmooth convex variational signal recovery. IEEE J of Sel Topics in Signal Process 1(4):564–574